doi:10.26443/seismica.v5i2.2150

Improving Tsunamigenic Source Models through Interseismic Coupling Approach in Stochastic Slip Distributions: Insights from Large Chilean Earthquakes

Alex Villarroel [1,8], **Ignacia Calisto** [*1], **Patricio Winckler** [2,5,6], **Javier Ruiz**[3], **Matthew Miller** [1], **Gonzalo Montalva** [4,7]

[1]Department of Geophysics, University of Concepción, Concepción, Chile, [2]Ocean Engineering School, University of Valparaíso, Valparaíso, Chile, [3]Department of Geophysics, Faculty of Physical and Mathematical Sciences, University of Chile, Santiago, Chile, [4]Civil Engineering Department, University of Concepción, Concepción, Chile, [5]Centro de Observación Marino para Estudios de Riesgos del Ambiente Costero (COSTA-R), Chile, [6]Centro de Investigación Interdisciplinaria en Riesgo, Resiliencia y Recuperación ante Desastres (CIGIDEN R+), Chile, [7]ACT240044 EASER: Evolution Assessment of Seismic Risk, [8]Department of Geology, Faculty of Physical and Mathematical Sciences, University of Chile, Santiago, Chile

Author contributions: *Conceptualization*: Ignacia Calisto, Alex Villarroel. *Methodology*: Alex Villarroel, Ignacia Calisto, Javier Ruiz, Gonzalo Montalva, Patricio Winckler, Matthew Miller. *Software*: Alex Villarroel. *Validation*: Alex Villarroel. *Formal Analysis*: Javier Ruiz, Patricio Winckler, Matthew Miller, Gonzalo Montalva. *Writing - Original draft*: Alex Villarroel. *Writing - Review & Editing*: Ignacia Calisto, Javier Ruiz, Patricio Winckler, Matthew Miller, Gonzalo Montalva. *Supervision*: Ignacia Calisto, Javier Ruiz, Patricio Winckler, Matthew Miller, Gonzalo Montalva.

Abstract Chile is one of the most seismically active countries in the world, having experienced three major earthquakes exceeding M_w 8.2 in 2010, 2014, and 2015. These tsunamigenic events provide critical observational constraints for developing realistic coseismic slip models. This study proposes a methodological framework to generate realistic stochastic slip distributions by incorporating interseismic coupling as prior information, along with physical constraints derived from the segmentation of the Chilean subduction margin and the seismogenic zone. Unlike purely unconstrained stochastic models, this approach narrows the solution space by applying a multistep selection filter to identify scenarios that are physically plausible and consistent with known rupture characteristics. The framework is applied to the Concepción, Valparaíso, and Iquique segments, generating tens of thousands of slip scenarios. Tsunami simulations based on the selected ensemble reproduced observed waveforms at multiple tide gauges. These scenarios achieved high cross-correlations in the first wavelength (≥ 0.85 in key stations) and root mean square error (RMSE) values comparable to established seismic inversion models. The results demonstrate that this constrained ensemble approach effectively quantifies uncertainty while producing physically plausible coseismic slip scenarios, offering an improvement for tsunami hazard assessment over deterministic or unconstrained stochastic methods.

Non-technical summary This study tests how incorporating interseismic coupling, a representation of how tectonic plates remain partially locked and accumulate deformation over time, can improve stochastic models of earthquake slip. By using this information to constrain the spatial patterns of slip, the models aim to better capture the complexity of earthquake rupture. The approach is evaluated by comparing simulated tsunamis with observations from recent Chilean earthquakes. Since it's impossible to know exactly where a future earthquake will start, generating many scenarios helps explore a wide range of possibilities. This approach allows the capacity to reproduce stochastic earthquake distributions and could support future hazard assessments.

Production Editor: Yen Joe Tan
Handling Editor: Wenbin Xu
Copy & Layout Editor: Anna M. Ledeczi

Received: 27 November 2025
Accepted: 9 November 2026
Published: 15 November 2026

1 Introduction

When a tsunamigenic earthquake occurs, the spatial distribution of slip on the fault plays a critical role in the generation and characteristics of the resulting tsunami. Therefore, to develop a statistical framework that could reproduce the rupture of an earthquake, stochastic coseismic slip distributions have been widely used for modeling the complexities of earthquake rupture (e.g Andrews, 1981; Herrero and Bernard, 1994; Mai and Beroza, 2002; LeVeque et al., 2016; Small and Melgar, 2021; Cifuentes-Lobos et al., 2023). The heterogeneities in large events are especially relevant for reproducing realistic near-field ground motions and for tsunami generation and propagation. In particular, generating heterogeneous slip distributions is fundamental for accurately characterizing tsunami estimated times of arrival (ETA) and amplitudes in both local and regional domains (Ruiz et al., 2015; Calisto et al., 2015; Melgar et al., 2019).

To better constrain the generation of realistic slip distributions for large earthquakes, we build upon a concept that has been explored in previous studies: the spatial relationship between coseismic slip and interseismic coupling. Interseismic coupling is defined here

*Corresponding author: icalisto@dgeo.udec.cl

as the ratio between the slip deficit rate on the plate interface and the long-term plate convergence rate, a dimensionless quantity ranging from 0, where the interface slips freely, to 1, where it is fully locked and the entire convergence is stored as elastic strain. The terms *seismic locking* and *locking degree* are used synonymously in the literature, whereas *interseismic slip deficit* denotes the dimensional quantity, that is, the slip that has not been released over a given time span. We follow the former usage throughout, noting that although coupling is well resolved by dense geodetic networks, its interpretation in terms of the mechanical behaviour of the fault remains unclear (Métois et al., 2016). This idea has been used to interpret past megathrust events, where regions of high slip often coincide with strongly coupled areas identified through geodetic observations. Moreno et al. (2010) showed that in the case of 2010 M_w 8.8 Maule earthquake, the prior distribution of interseismic coupling correlated with the future coseismic slip heterogenity at the scale of single asperities, proposing that the seismic potential of great earthquakes might be anticipated by geodetic observations. A year later, for the 2011 M_W 9.0 Tohoku earthquake, Loveless and Meade (2011) found agreement between the slip distribution and that of interseismic coupling. This conclusion has also been reached for the 2012 M_w 7.6 Nicoya earthquake (Protti et al., 2013). Based on this concept, Small and Melgar (2021) introduced interseismic coupling information into the stochastic slip distributions for the Cascadia subduction zone, discussing the comparison between models with and without a coupling constraint. Small and Melgar (2023) subsequently tested that comparison against a megathrust earthquake recorded in instrumental time, the 2011 M_w 9.1 Tohoku-Oki event, contrasting a homogeneous background model with two end-member coupling models: one improved the similarity to the published slip inversion, while the other produced no ruptures comparable to it. They concluded that, in the absence of a well-constrained coupling model, omitting the coupling constraint is the safer choice. This methodology has also been employed to determine coseismic slip characteristics in the 1920 M_s 8.5 Haiyuan Earthquake (Li et al., 2023), with a similar conclusion: depending on which coupling model was adopted as a prior, the fit to field-measured geomorphic offsets was either better or worse than that obtained with a uniformly coupled fault, even though the models compared were derived from the same GPS solution. Both studies thus point to the same requirement, that a coupling prior is advantageous only when the coupling model itself is well constrained.

Although the relationship between coupling and slip may be a first-order characteristic of a megathrust (Drápela et al., 2021), as visually illustrated for Chile in Figure 1b, an earthquake is governed by many other uncertain variables, such as complex fault geometries, past and present stress regimes, and rupture dynamics (Small and Melgar, 2021). This is precisely what makes the plausibility of the synthetic ruptures the central problem for hazard applications: a stochastic ensemble is only as informative as the ruptures it contains. Left unconstrained, the sampling spans slip patterns that the megathrust is unlikely to produce, and the resulting tsunami estimates carry a variability that does not originate in the fault; constrained too tightly, the ensemble collapses towards a single scenario and loses the exploration of the rupture space that motivates the stochastic approach in the first place. A set of ruptures is therefore considered realistic, in the sense used throughout this work, when it remains broad enough to sample the rupture space of a segment while reproducing the tsunami records of events that have already occurred there. Existing information about the seismotectonic setting of a given location offers a way to navigate between these two extremes: the spatial extent and magnitude of past earthquakes, the persistent barriers that limit rupture propagation along strike, and the downdip extent of the seismogenic zone can all serve as priors, alongside interseismic coupling.

As our aim is to use this prior information within specific segments in Chile, it is necessary to identify the properties of historical tsunamigenic events along the Nazca-South American plate subduction zone. The concept of earthquake segmentation refers to the division of a major fault system into partial segments that exhibit distinct mechanical behaviors during seismic cycles, where each segment may rupture independently, governed by variations in tectonic stress, frictional properties, rock compositions, topographic and bathymetric features (such as ridges or fracture zones) that may act as barriers. Particularly, the Chilean subduction zone is a global laboratory for segmentation research (Ely et al., 2014; Dura et al., 2015; Philibosian and Meltzner, 2020; Molina et al., 2021; Herrera et al., 2024), with at least six identified segments, delimited alongstrike by persistent, or broad persistent (overlap zones), barriers. In this study, we focus on the three segments where recent large megathrust earthquakes have been recorded by modern instrumentation: the Iquique segment, the Valparaíso segment, and the Concepción segment (Figure 1, orange, blue, and pink segments, respectively).

1.1 Iquique Segment

The north of Chile is considered a seismic gap with a high potential for the occurrence of a large earthquake (Hayes et al., 2014), with great earthquakes like those of 1768 (M unreported) and 1877 (M_s 8.5) earthquake that give a return period of 111 ± 33 years (Comte and Pardo, 1991), which to date has not yet fully released the accumulated seismic moment. The information on these historical seismic events contains greater uncertainties than to segments further to the north, as this region has sparse historical information due to the late settlement of colonized communities caused by geographical barriers such as the Atacama Desert and the lack of water (Comte and Pardo, 1991). Several works however estimate the approximate magnitude and rupture length of historical earthquakes from empirical relationships between intensity, magnitude and rupture length. Such historical events documented in the Iquique segment include the earthquakes of 1615(M_s 8.8), 1681 (M_s 7.3),

1768 ($MS(I)$ > 7.7), 1833 (M_s 7.7), 1836 (M_s 7.5), 1869 (M_s 7.5), 1871 (M_s 7.3), 1877 (M_s 8.5), and 1933 (M_s 7.6) (Comte and Pardo, 1991; Dorbath et al., 1990; Ruiz and Madariaga, 2018). However, to date, opinions remain divided whether the 1877 earthquake had the extent and magnitude as described; for example, Vigny and Klein (2022) revisited historical scientific articles to provide evidence about overestimations of the length and magnitude of the earthquake, estimating $M_w \sim 8.5$. On the other hand, Carvajal et al. (2025) calculated the magnitude and extent of the event using stochastic scenarios and compared it with the maximum wave heights caused by the tsunami in the far field, estimating M_w to lie between 8.8 and 8.9. Despite this large number of significant historical earthquakes, only those in 1615, 1877, and 2014 (M_w 8.2) were followed by reported tsunamis, leaving previous assumptions of the return period of interplate great events in this segment as, at least, questionable (Ruiz and Madariaga, 2018).

This long-standing hazard motivated extensive modern monitoring, for instance, the development of the IPOC network (GFZ German Research Centre For Geosciences and Institut Des Sciences De L'Univers-Centre National De La Recherche CNRS-INSU, 2006) in northern Chile in 2007. Geodetic studies using Global Positioning System (GPS) data acquired prior to 2014 revealed that the Iquique segment was highly coupled, having accumulated since the 1877 earthquake a moment deficit equivalent to a M_w 8.7 event, of which the 2007 Tocopilla earthquake had released only about 4% (Chlieh et al., 2011). On April 1, 2014, the M_w 8.2 Iquique earthquake partially ruptured this gap. Critically, detailed seismological and geodetic analyses showed that the 2014 event only broke the deeper portion of the locked zone and failed to rupture the shallowest, most strongly coupled patch where the largest slip occurred in 1877 (Schurr et al., 2014; Ruiz et al., 2014). Therefore, while the 2014 earthquake released a fraction of the accumulated strain, a substantial portion of the seismic moment deficit remains, especially at shallower depths. This leaves significant potential for a future great earthquake within the Iquique seismic gap (Hayes et al., 2014).

1.2 Valparaíso Segment

Moving further south to the central part of Chile (Figure 1), the Valparaíso segment is a highly active seismogenic zone. Its seismicity has been extensively documented since colonial times, due to the long-standing human settlements in the area. This region has experienced numerous significant historical earthquakes, including at least six events that generated moderate tsunamis: July 8, 1730 (M_w 9.0-9.3); November 19, 1822 (M_s 8.5); August 16, 1906 (M_w 8.2); April 6, 1943 (M_w 8.1); March 3, 1985 (M_w 8.0); and the most recent on September 16, 2015 (M_w 8.3). Among these, the 1730 earthquake stands out as a particularly large and shallow megathrust event, estimated at M_w > 9.0 (Carvajal et al., 2017), which also produced a destructive tsunami that severely impacted Valparaíso Bay.

The Valparaíso segment exhibits a wide variety of earthquake types, including interplate events in different structural domains, intermediate-depth intraplate earthquakes, shallow intraplate events, and even outer-rise events (Ruiz and Madariaga, 2018). The last significant earthquake in this region occurred on April 24, 2017, with a magnitude of M_w 6.9, which ruptured the shallow portion of the plate interface offshore of Valparaíso and was preceded by an intense foreshock sequence (Ruiz et al., 2017, 2018; Nealy et al., 2017). Currently, a significant seismic gap has been identified south of the 2017 earthquake rupture area (Nealy et al., 2017). This region exhibits a significant moment deficit, suggesting a high potential for a future large-magnitude earthquake. Estimated magnitudes range from M_w 7.8 to 8.2, and the magnitude could be even greater if pre-1900 strain accumulation (e.g., from the 1822 or 1730 events) contributes to the rupture size (Nealy et al., 2017).

1.3 Concepción Segment

Continuing further south to the central-southern part of Chile (Figure 1), the Concepción segment has historically been the source of numerous large-magnitude earthquakes, documented since colonial times. Among the most significant tsunamigenic events are those that occurred on February 8, 1570 ($M_s \sim 8.3$), which likely had an offshore epicenter and produced a tsunami with an initial upward surge prompting evacuation to high ground; March 15, 1657, where the tsunami flooded the main square of the city around 10 PM and caused multiple drownings; May 25, 1751 ($M_s \sim 8.5$), which caused widespread destruction and a large tsunami that ultimately led to the relocation of the city of Concepción to its present site; and February 20, 1835 ($M_s \sim 8.5$), famously observed by Charles Darwin, which triggered tsunami run ups up to 12 meters in Talcahuano Bay and was accompanied by significant coastal uplift (Lomnitz, 2004). The 27 February 2010 Maule earthquake (M_w 8.8) ruptured a seismic gap that had not broken since 1835, generating widespread damage and a significant tsunami (Moreno et al., 2010; Vigny et al., 2011; Lorito et al., 2011; Fritz et al., 2011). This segment exhibits a pattern of megathrust earthquakes with estimated recurrence intervals of 100–150 years, highlighting the persistent seismic hazard in the region (Beck et al., 1998).

1.4 Study Aims

This pattern of recurrent megathrust earthquakes in these segments underscores the relevance of understanding the segmentation and recurrence of tsunamigenic events along the Chilean margin. To reduce the uncertainties of location in historical earthquake documentation, detailed along-strike segmentation has also been identified through stochastic modeling of historical and paleo-tsunami sources (e.g. Cifuentes-Lobos et al., 2023; San Martín et al., 2024; Alvarez-Vargas et al., 2025). This modeling approach provides an approximation of the slip distribution in past events, revealing significant variability along strike and dip between earth-

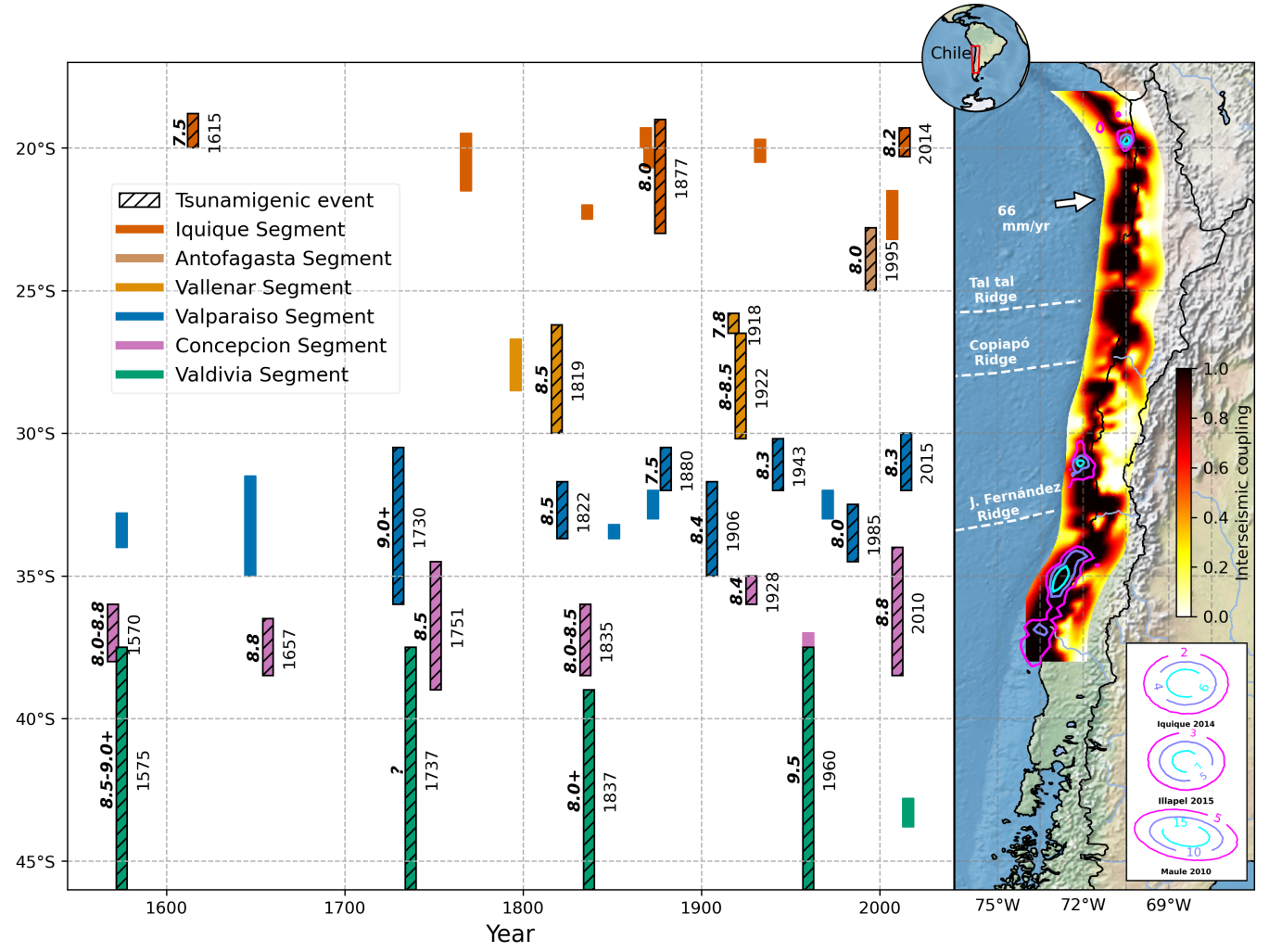


Figure 1 Historical seismic events and their approximate rupture lengths in Chile from 1500 to the present day, with fetch and magnitude for tsunamigenic events (data compiled in Philibosian and Meltzner, 2020), together with the map of interseismic coupling model for the Chilean subduction zone from Métois et al. (2016) and slip patterns of the 2010 M_w 8.8 Maule earthquake (Moreno et al., 2010), the 2014 M_w 8.2 Iquique earthquake (Hayes, 2017), and the 2015 M_w 8.3 Illapel earthquake (Hayes, 2017).

quakes, and suggesting that overlapping rupture areas may still exhibit different slip amounts. These findings support the hypothesis that each segment may not only rupture independently but also contribute differently to the tsunami generation depending on the specific slip distribution.

With these considerations, this study develops a framework to generate realistic stochastic slip scenarios for megathrust earthquakes, in which interseismic coupling enters as prior geophysical information and the rupture is bounded by physical constraints: the along-strike segmentation of the Chilean subduction margin and the downdip limit of the seismogenic zone. The framework is applied to the Concepción, Iquique and Valparaíso segments, using as prior magnitudes those of the 2010 Maule (M_w 8.8), 2014 Iquique (M_w 8.2) and 2015 Illapel (M_w 8.3) earthquakes, so that the resulting scenarios can be confronted with the tsunami records of events that actually occurred in each of them. Each ensemble is propagated as a tsunami and compared with tide gauge and DART observations, providing a quantitative measure of how well the simulated sources reproduce the recorded waveforms. To isolate the contribution of the coupling prior, the same procedure is repeated without the coupling constraint, and the two ensembles are compared both in the number of scenarios that meet the selection criteria and in their agreement with the observed waveforms.

The relevance of this framework lies in where it can be applied. The three events analysed here were chosen because they were recorded by modern instrumentation, which allows the simulated scenarios to be tested against observed tsunami waveforms. The segments of greatest concern, however, are those that have not ruptured in instrumental time, and it is precisely there that rupture scenarios must be constructed without a recorded event to base them on. Since interseismic coupling models are available along the entire Chilean margin, a framework validated where observations do exist can be transferred to segments where the earthquake has not yet occurred, supplying the physically constrained sets of sources on which tsunami hazard assessment and the estimation of expected wave amplitudes ultimately depend.

2 Methodology

2.1 Generation of Stochastic slip rupture

Stochastic slip rupture modeling treats the coseismic slip on a fault not as a single deterministic model, but as one realization of a spatially correlated random field. The field is defined by statistical properties inferred from slip inversions of past earthquakes: the amplitude of slip is described by a lognormal distribution, which guarantees positive values, and its spatial structure by an autocorrelation function whose correlation lengths along strike and dip scale with the dimensions of the rupture. The Karhunen-Loève expansion provides a way of constructing such a field, by decomposing the prescribed autocorrelation matrix into its eigenvalues and eigenvectors and combining them with a set of random coefficients, so that each set of coefficients yields a different slip distribution consistent with the same statistics. Repeating this sampling produces an ensemble of ruptures that share the same magnitude and the same statistical properties, but differ in the position and size of their asperities, and it is on this ensemble that the rest of this work operates. In what follows we describe how the domain and dimensions of the rupture are defined, how this field is constructed, and how the interseismic coupling model enters it.

Considering the prior information that we give to the model, the first step to generate stochastic slip distributions is to define a segment where seismic rupture can occur (Figure 2a). For this, the domain is set by making a non-regular mesh following the geometry of the slab given a specific region, determined by the along-strike segmentation (shown in Figure 1) and by the seismogenic zone along-dip. The strike, dip and subfault locations are interpolated from the Slab2 model (Hayes et al., 2018), and the rake is taken from NUVEL-1 (DeMets et al., 1990). Once the mesh is defined, the spatial slip distribution is restricted to be within the generated domain. The dimensions of the earthquake, length (L) and width (W), are determined by the magnitude, and there exist multiple linear scaling relationships between the logarithm of the dimensions and M_w (e.g. Blaser et al., 2010; Strasser et al., 2010; Goda et al., 2016). Taking in consideration the literature of rupture inversions of Mw 8+ earthquakes occurring along the Nazca-South American subduction margin, the Blaser et al. (2010) relation was used for rupture length and the Goda et al. (2016) relation for rupture width, using a truncated normal distribution ($\mathcal{N}_{trunc}$) with upper limits of L and W (L_{max} and W_{max}). The upper limits are controlled by the dimensions of the domain grid, restricted along-strike for the segmentation and along-dip for the seismogenic zone (We used a constant depth of 65 km). The samples of L and W are defined as,

$$\log_{10} L \sim \mathcal{N}_{\text{trunc}}\left(-2.37 + 0.57 M_w, \sigma_L, -\infty, \log_{10} L_{\max}\right) \tag{1}$$

$$\log_{10} W \sim \mathcal{N}_{\text{trunc}}\left(-0.49 + 0.31 M_w, \sigma_W, -\infty, \log_{10} W_{\max}\right) \tag{2}$$

where M_w is the moment magnitude of the earthquake, σ_L (0.1700 from Blaser et al., 2010) and σ_W (0.1717 from Goda et al., 2016) are the standard deviations for the length and width dimensions respectively.

Once the physical dimensions of the earthquake are determined, the stochastic spatial slip distribution is generated using the Karhunen-Loève expansion, following the methodology of LeVeque et al. (2016), with a lognormal expression that ensures positive slip values:

$$\vec{S} = \exp\left(\vec{\mu}^g\right) \exp\left(\sum_{k=1}^{m} z_k \sqrt{\lambda_k} \vec{v}_k\right) \tag{3}$$

where $\vec{S}$ is the final slip vector, $\vec{\mu}^g$ is the vector of log-mean slip (which incorporates the coupling constraint), and z_k are independent, normal random distributions with mean 0 and standard deviation 1. Furthermore, λ_k and $\vec{v_k}$ are the eigenvalues and eigenvectors, respectively, of the covariance matrix $\hat{C}^g_{ij} = \log\left(\alpha^2 C_{ij} + 1\right)$ (with $m = i \cdot j$), using the Von-Karman ACF (Mai and Beroza, 2002), $G_H(r_{ij})$, defined as:

$$G_H\left(r_{ij}\right) = r_{ij}^H K_H\left(r_{ij}\right) \tag{4}$$

$$C_{ij}\left(r_{ij}\right) = \frac{G_H\left(r_{ij}\right)}{G_0\left(r_{ij}\right)} \tag{5}$$

where C_{ij} is the correlation between the i-th and j-th subfaults, K_{H} is the modified Bessel function of the second kind, and H is the Hurst exponent. r_{ij} is the inter-subfault distance $r_{ij} = \sqrt{\left(r_s/a_s\right)^2 + \left(r_d/a_d\right)^2}$, with r_s and r_d as the distance between ij subfaults along strike and dip respectively, and a_s with a_d are the correlation lengths, obtained following the scaling law for great earthquakes from Melgar and Hayes (2019) based on effective dimensions (L_{eff} and W_{eff}), which could have a significant impact on the tsunami intensity measures (Crempien et al., 2020):

$$a_s = 17.7 + 0.35 * L_{eff} \tag{6}$$

$$a_d = 6.7 + 0.41 * W_{eff} \tag{7}$$

The interseismic coupling model (ϕ_i), as defined in the Introduction and illustrated in Figure 2b, is incorporated directly into the calculation of the log-mean slip (μ_i^g) for each subfault i. In the Karhunen-Loève expansion, the log-mean slip is defined by adapting the term that would typically serve as a geometrical *taper* with the normalized coupling model, rescaled to the interval $[0, 1]$ where the source model is reported as a percentage.

The log-mean slip is calculated as:

$$\mu_i^g = \log\left(\frac{\bar{\mu}_i \phi_i}{\sqrt{\alpha^2 + 1}}\right) \tag{8}$$

Here, $\bar{\mu}_i$ is the uniform average slip on subfault i required to satisfy the total seismic moment for the target earthquake magnitude M_w, as introduced by Aki (1966). This average slip accounts for the subfault's rigidity, which is inferred from its depth using the PREM model (Dziewonski and Anderson, 1981). The slip field is rescaled, after each stochastic realization, so that the

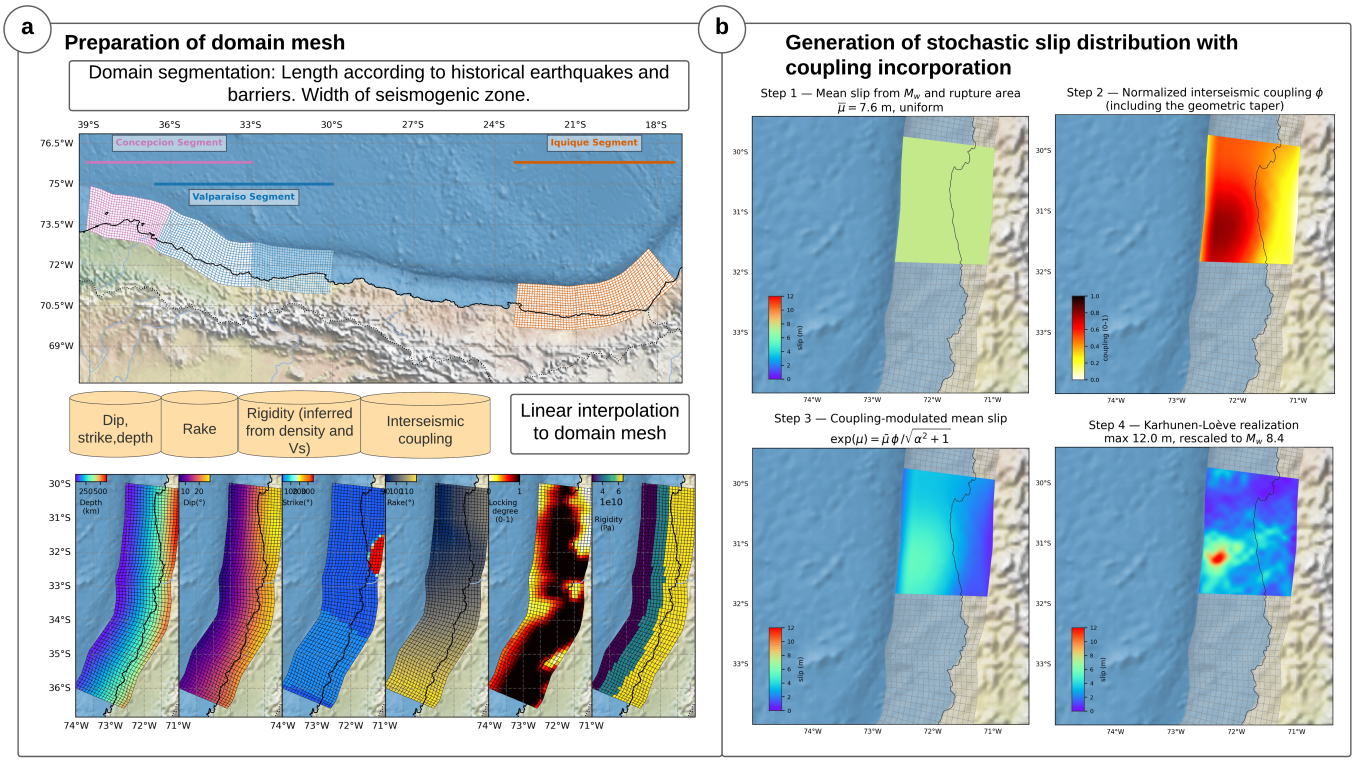


Figure 2 Workflow for the generation of stochastic slip distributions. (a) Preparation of the domain mesh, including segmentation of the seismogenic zone based on historical earthquakes and geological barriers. Fault parameters and interseismic coupling are interpolated to the computational mesh. (b) Generation of stochastic slip distributions using the Karhunen-Loève expansion constrained by interseismic coupling. The initial slip distribution (top left) is modulated by the normalized coupling map (bottom left), yielding a final slip distribution (right). Segment boundaries used in this study include Valparaíso, Concepción, and Iquique.

moment summed over the subfaults with their depth-dependent rigidity matches the target M_w. Every scenario of an ensemble therefore has exactly the target magnitude, and the variability of the ensemble lies entirely in the spatial distribution of slip and not in its total moment. The term ϕ_i is the normalized interseismic coupling at subfault i, and α is a constant (set to 0.5, following LeVeque et al., 2016). As described in the work of Small and Melgar (2021), This implementation ensures that the resulting stochastic slip distributions are constrained by the known interseismic coupling, meaning areas of high coupling are more likely to host larger slip, as described in Small and Melgar (2021) and shown in Figure 3.

Several interseismic coupling models overlap in each of the three segments studied here. The model used for the main ensemble of each event was chosen so that the geodetic data from which it is derived cover the interseismic period of that earthquake, that is, they predate it. A model inverted from velocities that include the post-seismic period already contains part of the signal of the rupture being reproduced, and using it as a prior would make the comparison with that same rupture circular. On this basis we use the model of Moreno et al. (2010) for the Concepción segment, Li et al. (2015) for the Iquique segment and Becerra-Carreño et al. (2022) for the Valparaíso segment. The remaining models were run as complete ensembles and their results are reported in the Supplementary Material, so that the effect of this choice can be assessed rather than assumed.

2.2 Selecting realistic scenarios of earthquake slip distributions

In order to select only cases where the slip distribution can reproduce plausible tsunamigenic earthquake scenarios, we defined certain rules with which to obtain the more geologically-realistic models (Figure 4). Once all simulations were completed, we extracted the maximum and mean slip, retaining only those within the interquartile range to exclude extreme values. Because slip distributions are expected to correlate with interseismic coupling, a minimum correlation threshold was imposed. The mode of the correlation coefficients, close to 0.5, was adopted as this threshold: it is the most frequent level of agreement produced by the coupling-constrained generation (Figure 3a), so adopting it retains the bulk of the ensemble while discarding the tail of scenarios that bear no relation to the coupling field. The threshold is a choice rather than a property of the method, and its consequences are examined in the Supplementary Material, together with the number of scenarios removed by each criterion. Furthermore, to be sure that the main patch is in a cumulative seismic moment asperity, it must be within a zone of high coupling. To obtain the distributions with high tsunami potential, we require that the main patch encompasses a zone which produces uplift of the ocean floor, although this constraint could be relaxed if the main slip patch

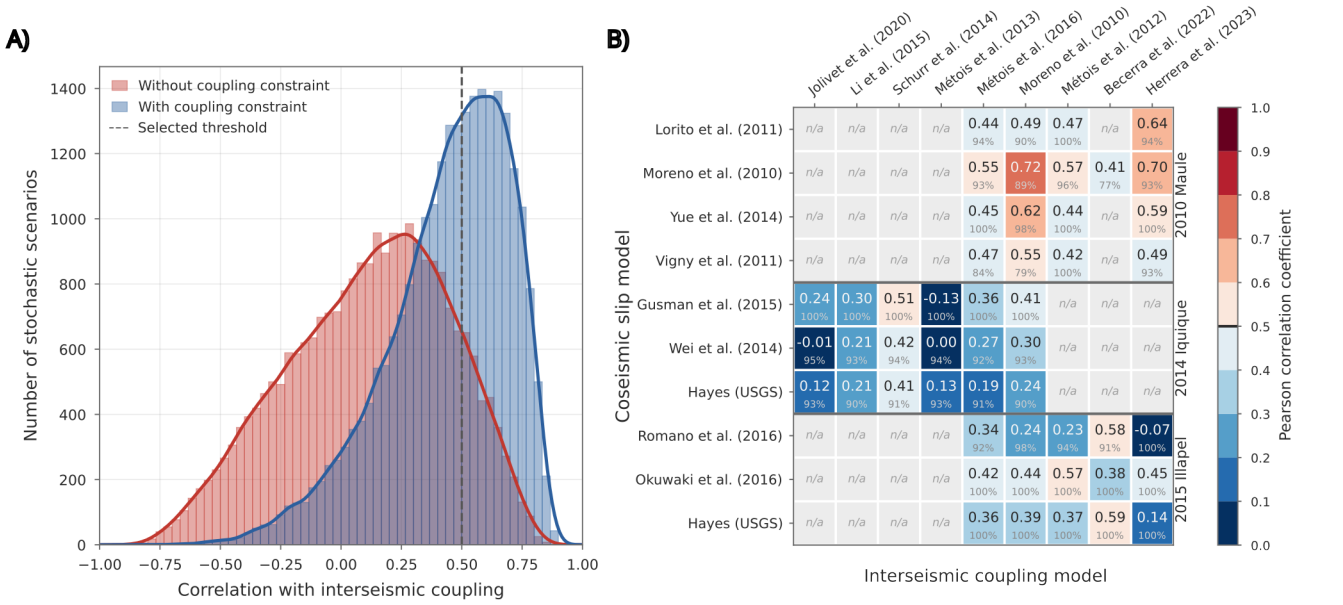


Figure 3 (a) Histogram of the correlation coefficient between stochastic slip distributions (with and without coupling constraint) and normalized interseismic coupling; the dashed line marks the threshold adopted for the selection of realistic scenarios. (b) Pearson correlation coefficient between published coseismic slip models and published interseismic coupling models, grouped by the 2010 Maule, 2014 Iquique, and 2015 Illapel earthquakes. The smaller number below each coefficient is the percentage of the slip model area covered by the corresponding coupling model; *n/a* indicates that the two models do not overlap.

is at greater depths, but there is a shallower secondary patch with tsunamigenic potential. Finally, so that the distribution does not break the physical principles of an earthquake, the distributions are subject to boundary conditions, where the edges cannot have the maximum slip values, excluding distributions with high slips near the trench, due the possibility of large slip at very shallow depth holds implications for up-dip strain accumulation and tsunamigenic earthquake potential of megathrusts elsewhere, such as the 2010 M_w 8.8 Maule, 2011 M_w 9.0 Tohoku, and 2015 M_w 8.3 Illapel earthquakes (e.g. Yue et al., 2014; Lay et al., 2011; Romano et al., 2016, respectively).

2.3 Tsunami modelling

The tsunami propagation was simulated using the parallel dispersive tsunami model PCOMCOT, which efficiently computes the full life cycle of nonlinear, dispersive, and breaking tsunami waves (Zhu et al., 2024). To ensure a physically realistic tsunami source, PCOMCOT applies the Kajiura filter to the initial surface deformation, which accounts for the low-pass filtering effect of seawater (Kajiura, 1963). We considered the earthquake rupture as instantaneous, because the rupture velocity is faster than the tsunami velocity. The vertical seafloor deformation was computed with the analytical solution of Okada (1985) for a rectangular dislocation in an elastic half-space, evaluated for each subfault and summed over the whole rupture. Additionally, the horizontal displacement of the seafloor was considered in the calculation of the sea surface deformation caused by earthquakes. The contribution of horizontal motion to seafloor uplift was calculated following the methodology of Tanioka and Satake (1996).

The simulations were conducted using 3 levels of nested grids with resolutions of 2.16, 0.54, and 0.108 arcminutes. Nonlinear effects were considered for the second and third levels of nested grids, however wave dispersion and breaking were not included.

2.4 Model Validation

To quantify how closely a simulated scenario resembles a published coseismic slip model, we use the dissimilarity D introduced by Small and Melgar (2023), based on the normalized square metric. For two slip distributions A and B interpolated onto a common regular grid of subfaults, it is defined as

$$D(A,B) = 100\,\frac{\sum_i \left[A(i)-B(i)\right]^2}{\left(\sum_i \left[A(i)\right]^2 + \sum_i \left[B(i)\right]^2\right)/2} \qquad (9)$$

where the sum runs over the subfaults of the common grid. D is expressed as a percentage: $D = 0$ denotes identical slip models, and the value grows with the difference between them, reaching 200 % when the two distributions have no overlap. We report D on this scale; note that Small and Melgar (2023) additionally divide it by two to obtain a range from 0 to 100. Because D compares two slip distributions rather than a model with an observation, it complements the waveform metrics described below, which compare the simulated tsunami with the tide-gauge records.

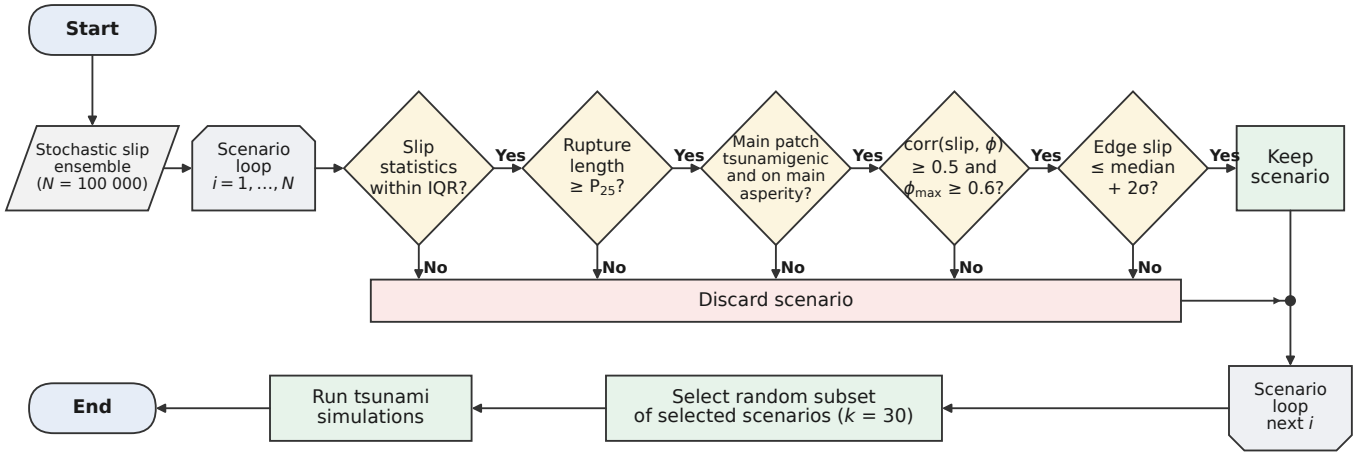


Figure 4 Flowchart for the selection of "potential" tsunamigenic earthquakes.

To compare the earthquake models with a model that has a good representation of tsunami wave arrivals and amplitude of the first wave, we used the Normalized Root Mean Square (NRMS) to compare the modelled tsunami signals against the observations of tidal gauges within a determined window time, which is the time that encloses the first wavelength of the tsunami signal. Also, we use the cross-correlation coefficient within this time window to find the best correlation of a model with the observation, and to evaluate if the time lag is within the 95% confidence interval of all the tsunami simulations. The NRMS is defined as follows,

$$\mathrm{NRMS} = \left[\frac{1}{o_{\max} - o_{\min}}\right] \sqrt{\frac{1}{L}\sum_{i=1}^{L}\left(o_i - v_{(i-l)}\right)^2} \qquad (10)$$

For a window length L, lag l, and observed and simulated signals o_i and v_i, respectively, while $o_{\max}$ and $o_{\min}$ are the maximum and minimum amplitude of the observed signal .

To compare the amplitude of the first tsunami wave, and following the procedure of Calisto et al. (2015), we adapt the SPGA (Similarity of Peak Ground Acceleration) that is a measure of similarity between the peaks of observed and synthetic seismic accelerations (Anderson, 2004), but as we are using the first peak of tsunami amplitude, we name SPTA (Similarity of Peak Tsunami Amplitude).

$$\mathrm{SPTA}(p_1, p_2) = 10 \exp\left\{-\left[\frac{(p_1 - p_2)}{\min(p_1, p_2)}\right]^2\right\} \qquad (11)$$

With p_1 and p_2 as the peaks of tsunami amplitude for signals 1 and 2, respectively, within the determined time window.

3 Results

3.1 2010 M_w 8.8 Maule Earthquake

To capture the main features of this event, 100,000 stochastic scenarios of magnitude M_w 8.8 were generated on the domain mesh of the Concepción segment (subfaults of 10 × 10 km), using the interseismic coupling model of Moreno et al. (2010). Of these, 741 passed all the selection criteria (0.7%; Figure 4), and a random subset of 30 was used for tsunami simulation, recording virtual tide gauges at Arica, Iquique, Buoy401, Buoy402, Coquimbo, Valparaíso, Talcahuano, Corral and Ancud. No observational records are available at the DART buoys 401 and 402 for this event, so at these two locations the ensemble can only be compared with the reference model and not with tsunami data.

The selected scenarios show asperities that vary in position and size within the tsunamigenic zone (Figure 5). Their median dissimilarity with the coseismic model of Lorito et al. (2011) is 42.5% (95% CI 41.6–43.4%), compared with 58.6% for scenarios generated and selected without coupling information; for reference, the published slip models of Moreno et al. (2010) and Yue et al. (2014) differ from Lorito et al. (2011) by 18% and 24%. The scenarios capture the main asperity of the earthquake especially well.

Figure 6 compares the median of the simulated tide-gauge records and their range with the observations, after applying the same 8–120 min band-pass filter to both. Averaged over the seven stations with records, the ensemble reaches NRMS = 0.24, SPTA = 6.15 and a lag-corrected correlation of 0.80; all four metrics are significantly better than for the ensemble without coupling information (NRMS 0.27, SPTA 4.75, correlation 0.77; bootstrap $p \leq 0.014$). For the first-wave window, the highest correlations ($R \geq 0.9$) are obtained at Coquimbo (0.93, 0.97 after a lag of 2 min) and Talcahuano (0.93, no lag), the latter evaluated until the gauge record is lost, 58 min after the earthquake. Ancud, Arica and Iquique reach correlations of 0.84–0.89 after lag correction, with lags of 0–8 min. In contrast, the model–data correlation at Corral remains low (0.37 after a lag of 12 min), suggesting a local effect not captured by the model or limitations of the slip distributions in that region. Regarding amplitude, the highest SPTA values are obtained at Talcahuano, Coquimbo, Iquique and Corral (SPTA > 8.4), whereas at Arica and Ancud the simulations do not reproduce the amplitude of the first wave (SPTA < 1). At Buoy401 and Buoy402, the ensemble me-

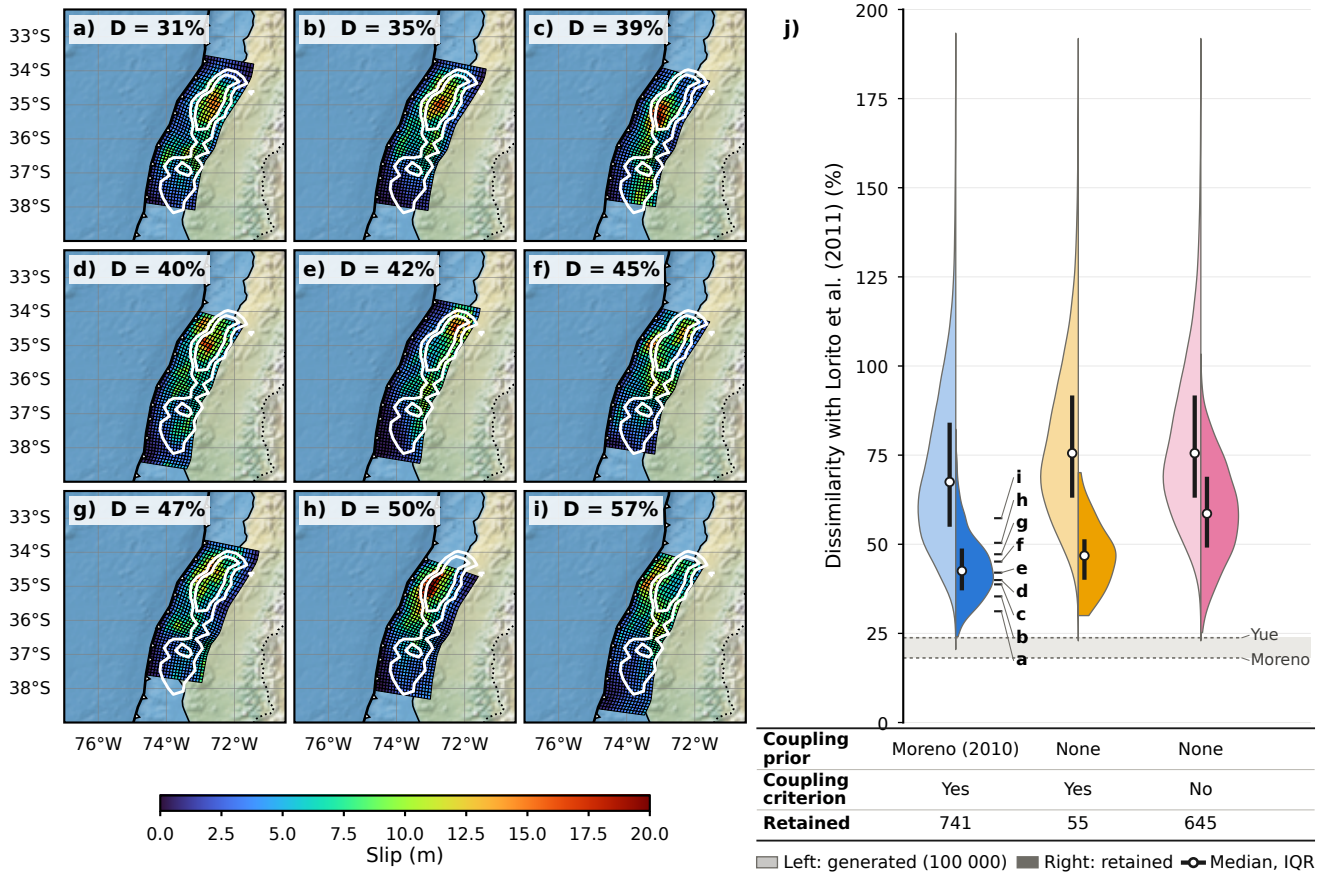


Figure 5 (a–i) Nine of the 30 retained scenarios used for tsunami simulation in the Concepción segment (coupling model of Moreno et al., 2010), chosen at evenly spaced quantiles of their dissimilarity D with the coseismic slip model of Lorito et al. (2011), from most to least similar. White lines: 5 and 10 m slip contours of Lorito et al. (2011). (j) Dissimilarity D with Lorito et al. (2011) of the scenarios generated with and without the coupling prior, retained with and without the coupling criterion (table below the panel): left half of each violin, all 100,000 generated scenarios; right half, scenarios retained by the selection criteria. Circles and bars: median and interquartile range; letters: scenarios shown in a–i. Grey band and dashed lines: D between Lorito et al. (2011) and the slip models of Moreno et al. (2010) and Yue et al. (2014). All 30 scenarios are shown in the Supplementary Material.

dian and the model of Lorito et al. (2011) yield consistent waveforms.

3.2 2014 M_w 8.2 Iquique Earthquake

For this event, 100,000 scenarios of M_w 8.2 were generated within the Iquique segment using the interseismic coupling model of Li et al. (2015). Following the selection criteria, the main slip patch was required to lie between 20.5°S and 19.5°S, in agreement with the location of the 2014 earthquake and considering that this area is bounded by low-coupling zones. A total of 536 scenarios passed all criteria (0.5%), and 30 of them were used for tsunami simulation. The selected scenarios sample the rupture space in a varied manner (Figure 7), mainly because this moderate-magnitude event has length and width smaller than the dimensions of the segment.

Iquique is the event where the method performs worst. The median dissimilarity of the selected scenarios with the model of Gusman et al. (2015) is 99%, and even the most similar of the 100,000 generated scenarios reaches 53%. This value should be read against the disagreement between published models of the same earthquake, which differ from Gusman et al. (2015) by 39% (Schurr et al., 2014), 86% (Hayes, 2017) and 96% (Wei, 2014). The compact rupture of the 2014 earthquake is resolved by few subfaults of the 10 km mesh, and the correlation lengths of the Karhunen–Loève expansion, derived from scaling laws, produce asperities larger than the main patch of the inversions.

At the tide gauges (Figure 8), the stations closest to the source show the best agreement: Iquique and Arica reach SPTA values of 10.0 and 9.9, NRMS of 0.15 and 0.12, and correlations of 0.94 after lags of 2 and 4 min. At Coquimbo and Talcahuano the ensemble underestimates the amplitude of the first wave (SPTA 2.4 and 2.6), although the lag-corrected correlations remain high (0.83 and 0.87, with lags of 12 and 14 min). At Valparaíso the amplitude agreement is good (SPTA 7.2), with the best correlation (0.77) at a lag of 18 min. The simulations at the DART buoys agree well with the model of Gusman et al. (2015) in amplitude, NRMS, correlation and lag. Corral and Ancud are not used in the metrics: at these distances the simulated tsunami amplitude (below 2 cm) is below the noise level of the records, and the first-wave window is truncated by the

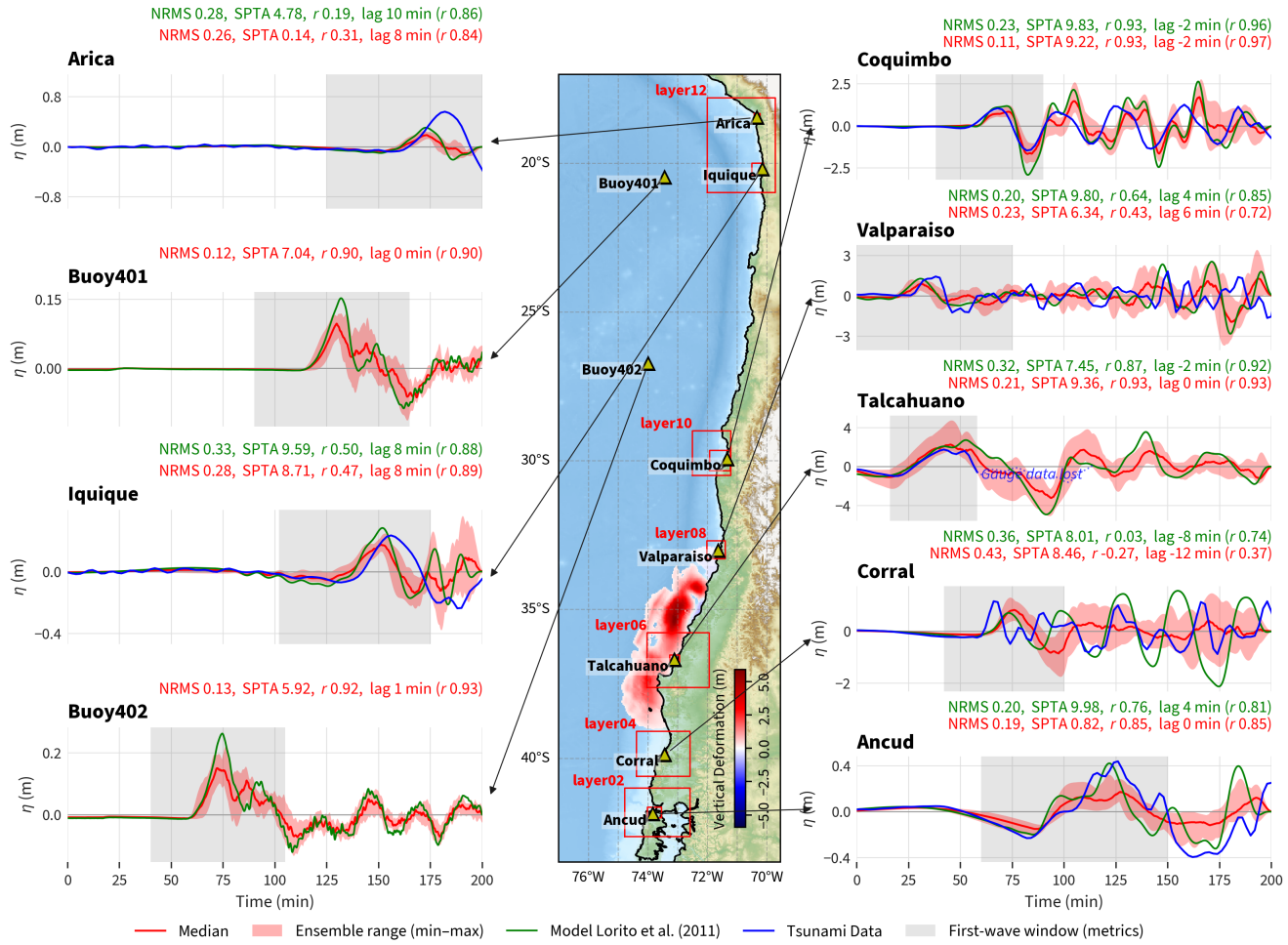


Figure 6 Bathymetric layer setup for tsunami modeling and vertical deformation of the 2010 earthquake (from Lorito et al., 2011), with tide-gauge records at Arica, Iquique, Buoy401, Buoy402, Coquimbo, Valparaíso, Talcahuano, Corral and Ancud, band-pass filtered between 8 and 120 min (DART buoys unfiltered). Blue: observed tsunami data from the IOC Sea Level Station Monitoring Facility (Flanders Marine Institute (VLIZ), Belgium and Intergovernmental Oceanographic Commission-UNESCO, France, 2021); green: simulation from the slip model of Lorito et al. (2011); red: median of the 30 stochastic scenarios and their range (minimum–maximum). Grey band: first-wave window used for the metrics. Metrics (NRMS, SPTA, correlation and optimal lag) are shown for the reference model (green) and the ensemble median (red). At Talcahuano the gauge record is lost 58 min after the earthquake (dotted line).

simulation length. Averaged over the five remaining stations, the ensemble does not differ significantly from the one generated without coupling information in any metric (SPTA 6.43 versus 6.29, $p = 0.95$).

3.3 2015 M_w 8.3 Illapel Earthquake

In this case, 100,000 scenarios of M_w 8.3 were generated using the interseismic coupling model of Becerra-Carreño et al. (2022), which is based on geodetic data acquired before the 2015 earthquake. A total of 1,445 scenarios passed all criteria (1.4%), and 30 were used for tsunami simulation.

The selected slip distributions (Figure 9) exhibit considerable spatial variability and reveal the difficulty of sampling solutions with high slip near the trench, likely because of the limited spatial resolution and the smoothing inherent in the inversion of interseismic coupling models. Their median dissimilarity with the model of Romano et al. (2016) is 63%, compared with 98% without coupling information; published models of this earthquake differ from Romano et al. (2016) by 44% (Hayes, 2017) and 47% (Okuwaki et al., 2016). Among the coupling models tested for this segment, the model of Becerra-Carreño et al. (2022) produced the scenarios most similar to the coseismic inversions (median D of 82% for the compilation of coupling models and 94% for Métois et al., 2016).

At the tide gauges (Figure 10), Talcahuano shows the best agreement (NRMS 0.08, SPTA 9.7, correlation 0.98 without lag), followed by Iquique and Arica (SPTA 10.0 and 9.6, lag-corrected correlations 0.91 and 0.76). At Coquimbo, the closest station to the rupture, the ensemble underestimates the amplitude of the first wave (SPTA 5.4) but reproduces its shape (correlation 0.94 after a lag of 6 min); this is consistent with simulated slip distributions that tend to concentrate closer to the coast than the inversion models, which suggest rupture propagation toward the trench. Corral simulations underestimate the amplitude (SPTA 3.5), and Ancud is not used

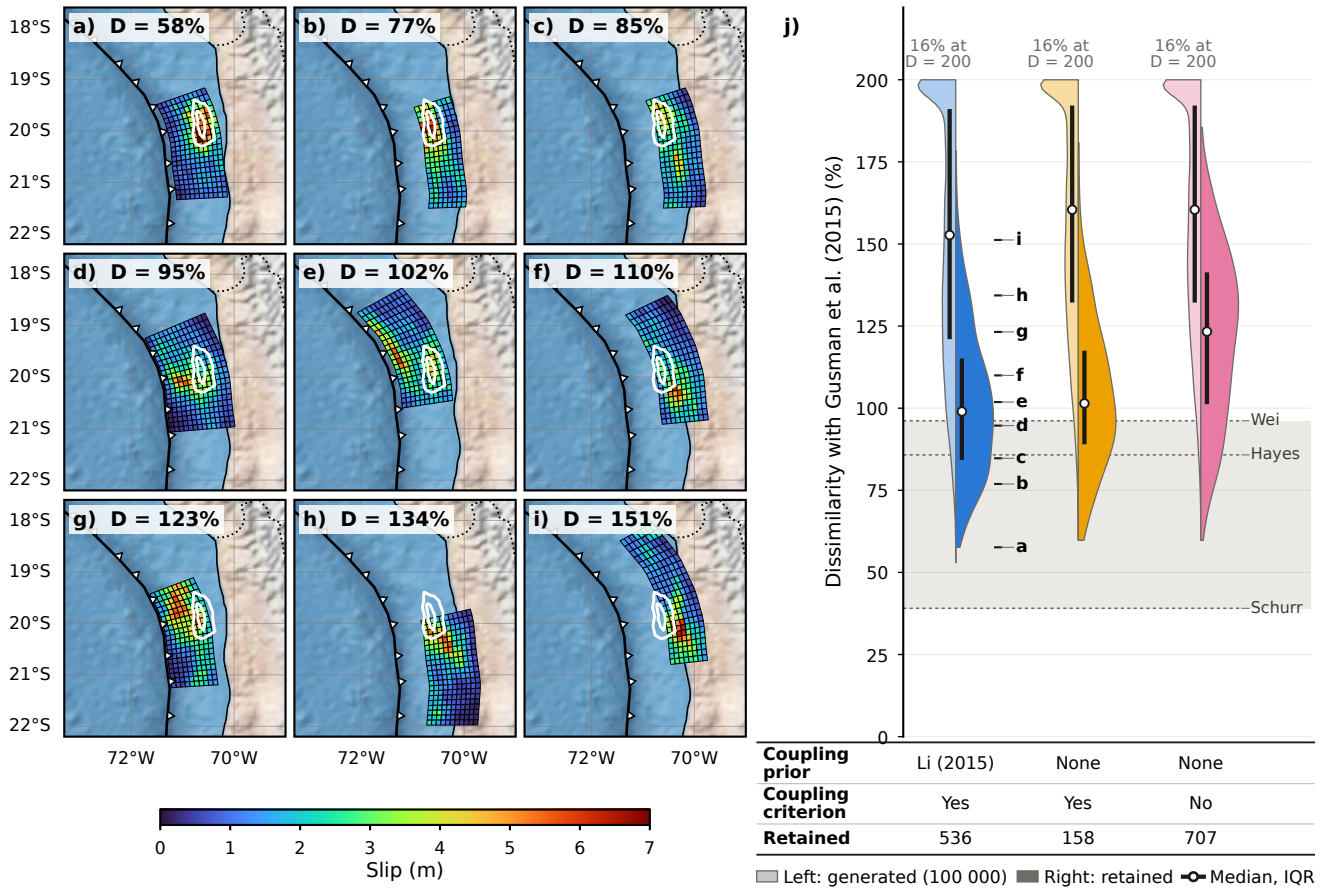


Figure 7 (a–i) Nine of the 30 retained scenarios used for tsunami simulation in the Iquique segment (coupling model of Li et al., 2015), chosen at evenly spaced quantiles of their dissimilarity D with the coseismic slip model of Gusman et al. (2015), from most to least similar. White lines: 2 and 4 m slip contours of Gusman et al. (2015). (j) Dissimilarity D with Gusman et al. (2015) of the scenarios generated with and without the coupling prior, retained with and without the coupling criterion (table below the panel): left half of each violin, all 100,000 generated scenarios; right half, scenarios retained by the selection criteria. Circles and bars: median and interquartile range; letters: scenarios shown in a–i. $D = 200\%$ indicates no overlap with the reference model; the fraction of generated scenarios at this value is given above each violin. Grey band and dashed lines: D between Gusman et al. (2015) and the slip models of Schurr et al. (2014), Hayes (2017), and Wei (2014). All 30 scenarios are shown in the Supplementary Material.

in the metrics because the tsunami signal cannot be isolated within the simulation length. The DART buoy simulations agree well with the model of Romano et al. (2016), with optimal lags of at most 2 min (SPTA 9.7 and 9.3). Averaged over the six stations used, the ensemble reaches SPTA = 7.55 and a lag-corrected correlation of 0.86, both significantly better than without coupling information (SPTA 5.41, correlation 0.79; $p \leq 0.007$).

4 Discussion

Given the objective of this study to capture the main features of a tsunamigenic earthquake by incorporating interseismic coupling into the stochastic modeling, we have analyzed the similarity between the simulated scenarios and tsunami data inversions. To anchor our stochastic simulations within the long-term tectonic context, we impose a correlation constraint between the generated slip distributions and a model of interseismic coupling. This methodological choice ensures that our scenarios preferentially represent earthquakes where slip is largely governed by pre-existing locked patches. However, we acknowledge this approach introduces a dependency on the chosen interseismic coupling model and may systematically exclude less-correlated but physically plausible rupture scenarios, a limitation that must be considered when interpreting the resulting tsunami hazard. For example, as illustrated in Figure 1 and in Figure 3b, it becomes evident that achieving realistic slip distributions via correlation strongly depends on the geodetic inversion, or the InSAR-derived interseismic coupling models. That agreement is moreover strongly region-dependent: for the 2010 Maule earthquake the correlation between published slip and coupling models ranges from 0.41 to 0.72, whereas for the 2014 Iquique earthquake only one of the eighteen pairs reaches 0.5, and for the 2015 Illapel earthquake only two do. In those two segments our criterion therefore asks the synthetic scenarios to agree with the coupling model more closely than the published inversions of the real earthquakes do, which over-constrains the ensemble and is part of why the

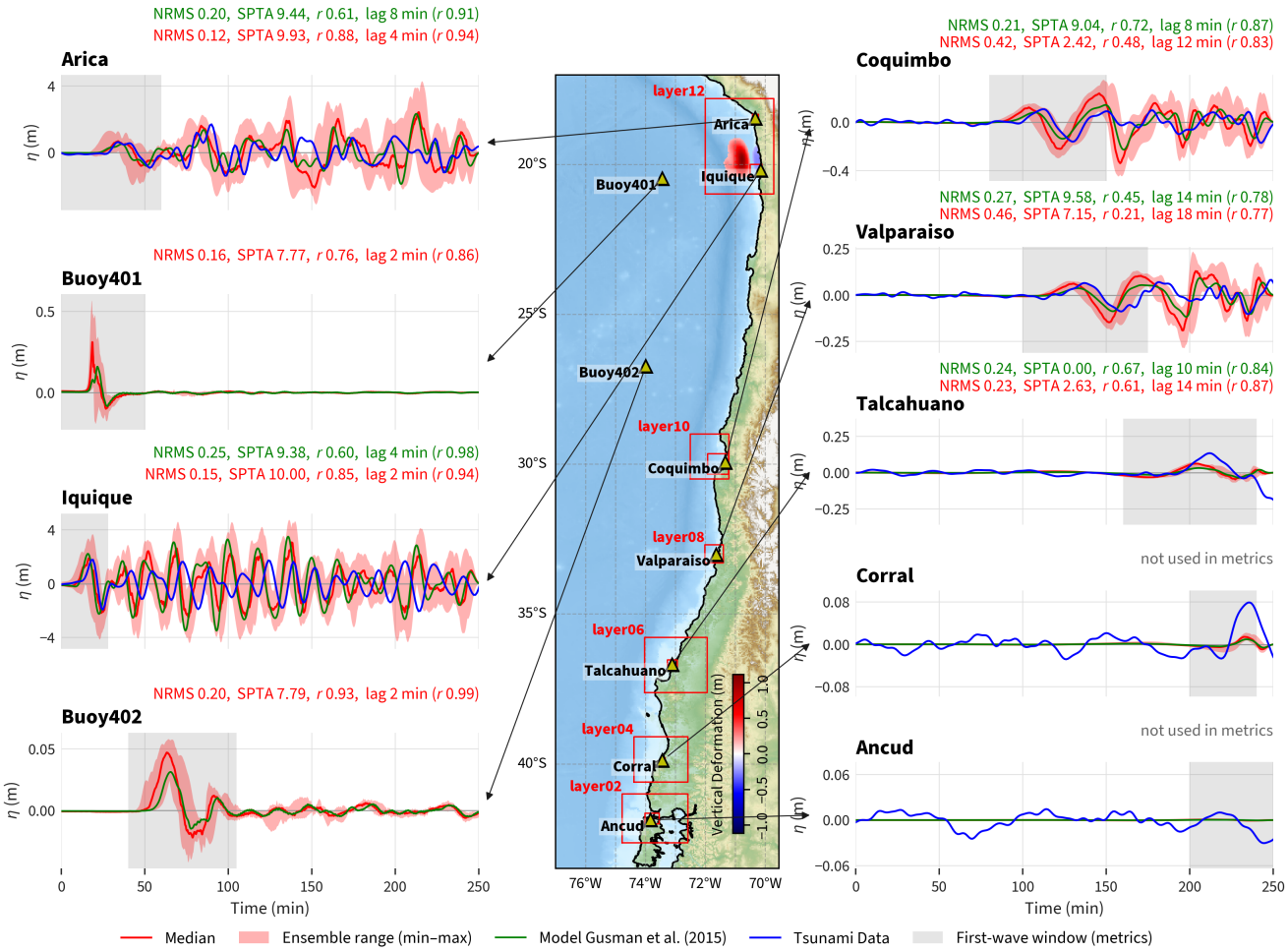


Figure 8 Same as Figure 6 for the 2014 Iquique earthquake, with vertical deformation and reference simulation from the slip model of Gusman et al. (2015). Corral and Ancud are not used in the metrics.

method performs worst at Iquique. We therefore suggest that the correlation threshold should not be kept as a single global value, but set from the slip–coupling agreement observed in each margin; where no recorded earthquake is available against which to measure it, a lower threshold is the safer choice, since it widens rather than narrows the set of scenarios considered possible.

Our analysis shows that the simulations over the Concepción segment tend to capture the main asperity of the 2010 Maule earthquake well, whereas the secondary asperity near Arauco is less accurately represented. In this segment, we have used the interseismic coupling model presented by Moreno et al. (2010) as the basis for our simulations. However, a more recent study that incorporates uncertainty in the coupling estimates for this region prior to the earthquake (Becerra-Carreño et al., 2022) indicates that the 2010 earthquake nucleated in a highly coupled area. Interestingly, the largest slip concentrations occurred in regions where the coupling decreased to approximately 0.6, although this observation remains uncertain as more recent studies than that of Lorito et al. (2011), such as Yue et al. (2014) and Maksymowicz et al. (2015), suggest that the maximum slips are closer to the trench than initially believed, precisely where the interseismic coupling models are most uncertain. This may suggest that a slip deficit still remains in the highly coupled zone. Moreover, it raises the possibility that the largest co-seismic slips tend to occur in regions that are neither strongly nor weakly coupled, but rather in areas of intermediate coupling, or simply that we are not yet able to characterize the coupling near the trench sufficiently well.

On average, the results showed a good fit for the first wave at the tide gaude stations located within the rupture area, which are the most affected due to their proximity to the main asperities. Corral station, located at the mouth of the Valdivia River showed the worst correlation with the first tsunami wave, which could be attributed to a low-resolution or inaccurate bathymetric model near Corral or unmodeled local effects or tide-tsunami interactions (Winckler et al., 2017).

Our findings exhibit that the distributions of the simulations of Iquique and Valparaíso segments tend to exhibit greater spatial uncertainty, due to their smaller rupture size, which inherently leads to more scattered sampling within the segment domain. Nevertheless, the average size of the asperities, dependent on the autocorrelation matrix determined by the correlation lengths, is comparable to that of the main asperities of observed earthquakes, suggesting coherence in the stochastic generation of slip distributions. For the 2015

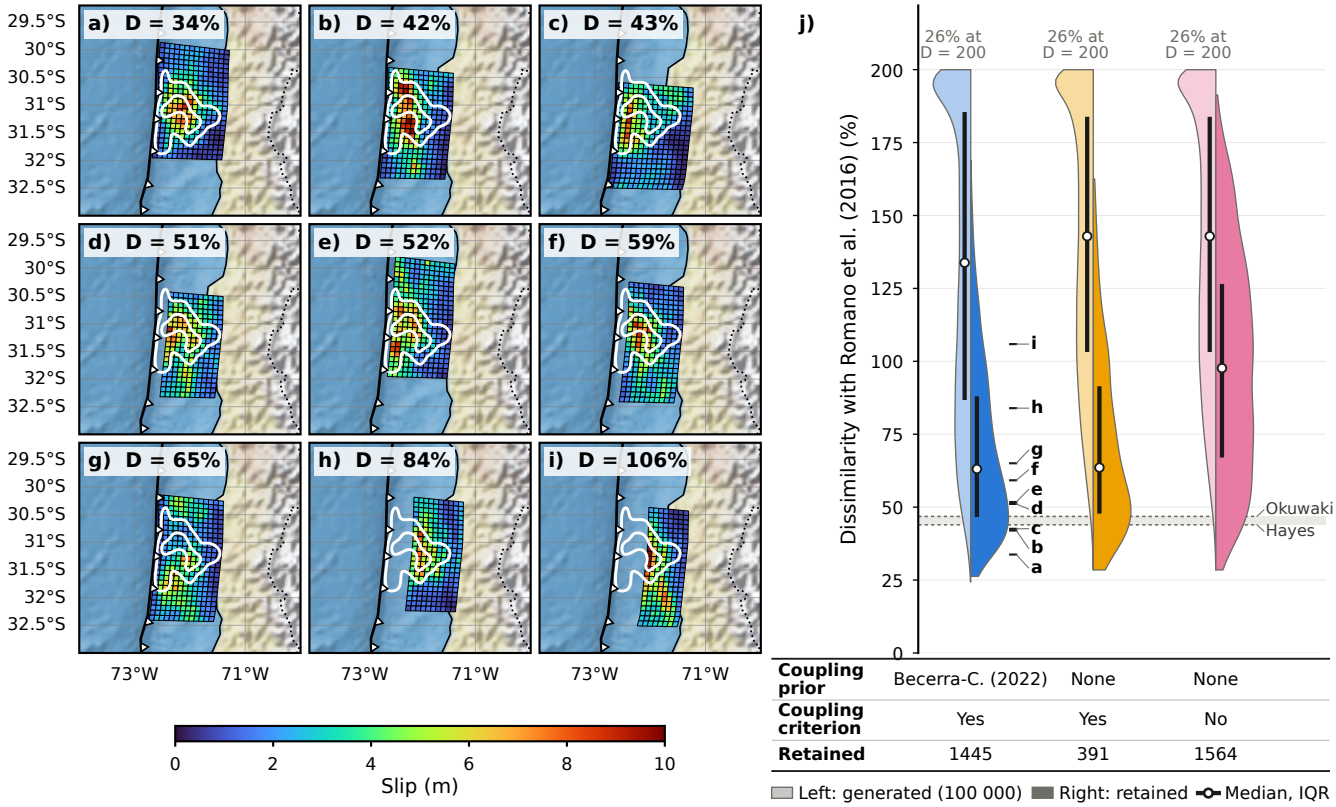


Figure 9 (a–i) Nine of the 30 retained scenarios used for tsunami simulation in the Valparaíso segment (coupling model of Becerra-Carreño et al., 2022), chosen at evenly spaced quantiles of their dissimilarity D with the coseismic slip model of Romano et al. (2016), from most to least similar. White lines: 3 and 6 m slip contours of Romano et al. (2016), smoothed with a 10 km Gaussian filter for display only (D is computed from the original model). (j) Dissimilarity D with Romano et al. (2016) of the scenarios generated with and without the coupling prior, retained with and without the coupling criterion (table below the panel): left half of each violin, all 100,000 generated scenarios; right half, scenarios retained by the selection criteria. Circles and bars: median and interquartile range; letters: scenarios shown in a–i. D = 200% indicates no overlap with the reference model; the fraction of generated scenarios at this value is given above each violin. Grey band and dashed lines: D between Romano et al. (2016) and the slip models of Hayes (2017) and Okuwaki et al. (2016). All 30 scenarios are shown in the Supplementary Material.

Illapel Earthquake simulations, a smaller number of selected distributions coincide with high amounts of slip in the trench, which suggests inferior performance of the interseismic coupling implementation compared to the other segments analyzed, determined mainly by the interseismic coupling model used, smoothed, and with more uncertainties near the trench.

Comparing our approach with Small and Melgar (2021) and Small and Melgar (2023), who highlighted the importance of incorporating interseismic coupling patterns into stochastic rupture modeling and showed that coupling-conditioned ruptures lead to variable tsunami hazards, our work follows a similar route but focuses on the Chilean subduction zone and is validated against observed tidal data from three different earthquakes. Unlike their broader probabilistic sampling, we introduced stricter selection constraints based on interseismic coupling and geophysical context. This results in a substantially reduced number of simulations passing the selection criteria, narrowing the range of plausible rupture scenarios while still capturing the key features of the main asperities. Consequently, our approach aims to generate a model capable of realistically reproducing tsunamigenic scenarios, grounded in observed events, highlighting the trade-off between model realism and scenario diversity.

A further limitation concerns the assumption, implicit in using coupling as a prior, that the locked state of the interface is stationary. Interseismic coupling is not static: it varies over the earthquake cycle, and geodetic records long enough to resolve that variation show it directly. Loveless and Meade (2016) inverted two decades of GNSS data offshore Japan in five consecutive epochs and imaged changes in the extent and degree of coupling associated with successive megathrust earthquakes, and Abe and Yoshioka (2022) resolved the coupling of the Tohoku segment annually over the fourteen years preceding the 2011 earthquake. A coupling model therefore represents the state of the interface during its observation window, and both the extent of the locked zone and its degree of coupling may differ between that window and the earthquake. Where that difference is large, the prior will steer the scenarios towards a configuration that no longer holds, and the constraint will be misleading rather than merely weak. The models used here are all derived from data that predate the earth-

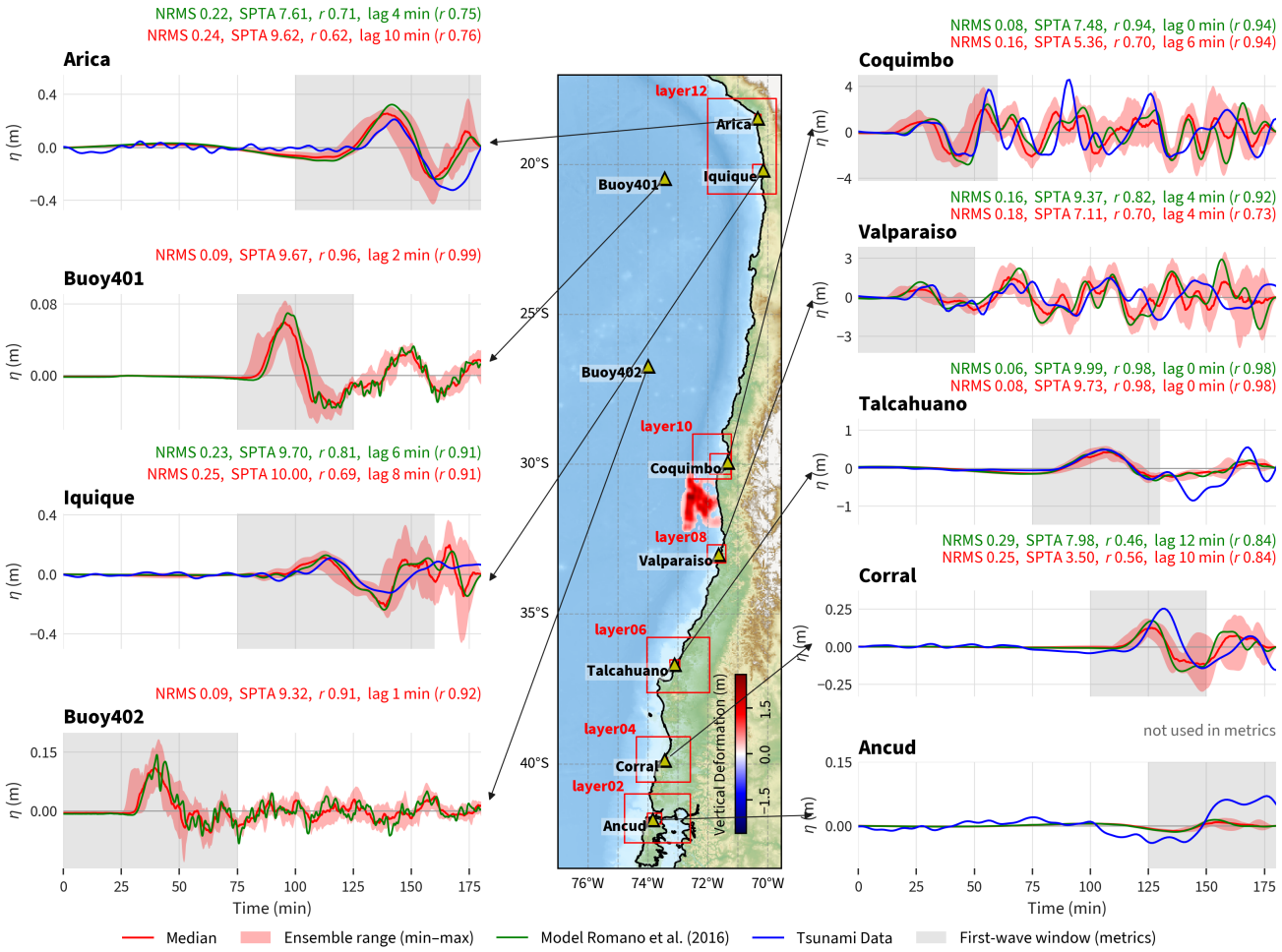


Figure 10 Same as Figure 6 for the 2015 Illapel earthquake, with vertical deformation and reference simulation from the slip model of Romano et al. (2016). Ancud is not used in the metrics.

quake they are applied to, which removes the circularity of including the post-seismic signal but does not remove this limitation. Along the Chilean margin the geodetic record is not yet long or dense enough to resolve the temporal variation of coupling in the way it has been resolved offshore Japan, and doing so would require a sustained extension of the offshore and onshore networks.

Finally, the relationship between interseismic coupling and rupture areas is particularly important, and thus improving instrumental coverage could significantly enhance our understanding of the seismic cycle and rupture patterns, especially along the dip direction, in regions near the trench, where offshore instrumentation has not been developed yet, and is essential to prepare for the next large earthquake.

5 Conclusions

This work introduces a stochastic modeling framework that incorporates depth-dependent average slip for each subfault and leverages the Karhunen-Loève expansion to integrate interseismic coupling using the same mathematical properties as a slip taper. Rupture boundaries are defined by margin segmentation along strike and by the seismogenic zone along dip, both strongly influenced by interseismic coupling. Despite these constraints, uncertainties remain that do not preclude the occurrence of an earthquake capable of breaking a persistent barrier. A deeper understanding of the seismotectonic structure of the subduction zone and the likely maximum magnitude could further help to limit these uncertainties.

Overall, this study demonstrates the potential of integrating interseismic coupling into stochastic earthquake modeling to generate realistic tsunamigenic scenarios. The proposed framework successfully reproduced key rupture features, such as the main asperities of large Chilean subduction earthquakes, while capturing the spatial variability inherent to each segment. The tsunami modeling results further support the validity of this approach, as the simulated waveforms matched well with the observed first wave arrivals at most stations. Considering that the analyzed earthquakes occurred in highly coupled regions, this coupling-informed stochastic approach provides a means of constraining potential earthquake sources and identifying plausible rupture scenarios within seismic gaps. However, uncertainties persist due to the limited offshore geodetic coverage and the dependence on prior coupling information. Because the magnitude is fixed at the published value of each event so that the simulated waveforms can be confronted with the

records, the ensembles presented here do not sample magnitude at all. Expanding the stochastic simulation set to encompass a broader range of magnitudes, maximum slip locations, and subsegment configurations are necessary to enhance the probabilistic representation of tsunamigenic hazards and improve the predictive capacity of future assessments along the Chilean or another subduction margin.

6 Acknowledgements

We gratefully acknowledge the support of the Geophysics Master's program of the University of Concepción, and the Servicio Hidrográfico y Oceanográfico de la Armada de Chile (SHOA) for providing the nautical chart used to build the high-resolution bathymetry of the Valparaíso region. We sincerely thank David Small for his detailed and constructive review, which substantially improved this manuscript.

7 Data and code availability

The interseismic coupling models used as priors were taken from Moreno et al. (2010) for the Concepción segment, Li et al. (2015) for the Iquique segment and Becerra-Carreño et al. (2022) for the Valparaíso segment; the models of Métois et al. (2016) and Schurr et al. (2014) were additionally tested and are reported in the Supplementary Material.

The published coseismic slip models used as references for the dissimilarity metric are those of Lorito et al. (2011), Moreno et al. (2010) and Yue et al. (2014) for the 2010 Maule earthquake, Gusman et al. (2015) and Schurr et al. (2014) for the 2014 Iquique earthquake, and Romano et al. (2016) and Okuwaki et al. (2016) for the 2015 Illapel earthquake, together with the finite-fault solutions of the USGS (Hayes, 2017) and the Caltech Tectonics Observatory (Wei, 2014). These models are distributed through the SRCMOD database, whose records remain accessible through the EMSC service at https://www.seismicportal.eu/srcmodws/.

Tide-gauge records were obtained from the IOC Sea Level Station Monitoring Facility (Flanders Marine Institute (VLIZ), Belgium and Intergovernmental Oceanographic Commission-UNESCO, France, 2021). The fault geometry was interpolated from Slab2 (Hayes et al., 2018), the rake from NUVEL-1 (DeMets et al., 1990) and the rigidity from PREM (Dziewonski and Anderson, 1981). The bathymetry of the coarser nested grids derives from the GEBCO global grid, and that of the finest grid in the Valparaíso region from a nautical chart provided by SHOA. The bathymetric grids actually used in the simulations are included in the repository, so that the runs can be reproduced exactly.

Tsunami propagation was computed with PCOMCOT (Zhu et al., 2024), and all maps and figures were generated with Cartopy (Met Office, 2010 - 2015). The codes used to generate, select and compare the stochastic slip scenarios, together with the selected scenarios of the three segments, are available at https://doi.org/10.5281/zenodo.17651149.

8 Competing interests

The authors declare that there are no known financial or personal conflicts of interest that could have influenced the work reported in this paper.

References

Abe, D. and Yoshioka, S. Spatiotemporal distributions of interplate coupling in Tohoku, northeast Japan, for 14 years prior to the 2011 Tohoku-oki earthquake inverted from GNSS data. *Tectonophysics*, 838:229479, 2022. doi: 10.1016/j.tecto.2022.229479.

Aki, K. Generation and propagation of G waves from Niigata earthquake of June 16, 1964, II, Estimation of earthquake moment, released energy, and stress-strain drop from the G wave spectrum. *Bull. Earthquake Res. Inst. Univ. Tokyo*, 44:73–88, 1966.

Alvarez-Vargas, J., Calisto, I., Faccenna, C., Cifuentes-Lobos, R., Cortés-Aranda, J., and Araya, R. Megathrust earthquake characterization along the central Chile Gap: Exploring Historical Earthquakes Using the Stochastic Logic Tree Approach. *ESS Open Archive (preprint)*, Feb. 2025. doi: 10.22541/essoar.173870826.69938280/v1.

Anderson, J. Quantitative measure of the goodness-of-fit of synthetic seismograms. In *Proceedings of the 13th World Conference on Earthquake Engineering*, pages 1–6, Vancouver, B.C., Canada, Aug. 2004. Earthquake Engineering Research Institute.

Andrews, D. J. A stochastic fault model: 2. Time-dependent case. *Journal of Geophysical Research: Solid Earth*, 86(B11): 10821–10834, Nov. 1981. doi: 10.1029/jb086ib11p10821.

Becerra-Carreño, V., Crempien, J. G. F., Benavente, R., and Moreno, M. Plate-Locking, Uncertainty Estimation and Spatial Correlations Revealed With a Bayesian Model Selection Method: Application to the Central Chile Subduction Zone. *Journal of Geophysical Research: Solid Earth*, 127(10), Oct. 2022. doi: 10.1029/2021jb023939.

Beck, S., Barrientos, S., Kausel, E., and Reyes, M. Source characteristics of historic earthquakes along the central Chile subduction Askew et alzone. *Journal of South American Earth Sciences*, 11 (2):115–129, Mar. 1998. doi: 10.1016/s0895-9811(98)00005-4.

Blaser, L., Kruger, F., Ohrnberger, M., and Scherbaum, F. Scaling Relations of Earthquake Source Parameter Estimates with Special Focus on Subduction Environment. *Bulletin of the Seismological Society of America*, 100(6):2914–2926, Dec. 2010. doi: 10.1785/0120100111.

Calisto, I., Ortega, M., and Miller, M. Observed and modeled tsunami signals compared by using different rupture models of the April 1, 2014, Iquique earthquake. *Natural Hazards*, 79(1): 397–408, June 2015. doi: 10.1007/s11069-015-1848-x.

Carvajal, M., Cisternas, M., and Catalán, P. A. Source of the 1730 Chilean earthquake from historical records: Implications for the future tsunami hazard on the coast of Metropolitan Chile. *Journal of Geophysical Research: Solid Earth*, 122(5):3648–3660, May 2017. doi: 10.1002/2017jb014063.

Carvajal, M., Gubler, A., Davies, G., Wang, K., Sun, T., and Catalán, P. A. Large Size of Two 19th-Century Chile-Peru Earthquakes Inferred From Trans-Pacific Tsunami Records. *Geophysical Research Letters*, 52(12), June 2025. doi: 10.1029/2024gl113849.

Chlieh, M., Perfettini, H., Tavera, H., Avouac, J.-P., Remy, D., Nocquet, J.-M., Rolandone, F., Bondoux, F., Gabalda, G., and Bonvalot, S. Interseismic coupling and seismic potential along the Central Andes subduction zone. *Journal of Geophysical Research*, 116(B12), Dec. 2011. doi: 10.1029/2010jb008166.

Cifuentes-Lobos, R., Calisto, I., MacInnes, B., Moreno, M., Quezada,

J., San Martín, J., Fernández-Palma, M., and Saavedra, C. A stochastic approach to the characterization of the seismic sources: a potential method for the assessment of sources of historical and paleo tsunami. *Stochastic Environmental Research and Risk Assessment*, 37(7):2399–2411, Mar. 2023. doi: 10.1007/s00477-023-02397-1.

Comte, D. and Pardo, M. Reappraisal of great historical earthquakes in the northern Chile and southern Peru seismic gaps. *Natural Hazards*, 4(1):23–44, 1991. doi: 10.1007/bf00126557.

Crempien, J. G. F., Urrutia, A., Benavente, R., and Cienfuegos, R. Effects of earthquake spatial slip correlation on variability of tsunami potential energy and intensities. *Scientific Reports*, 10 (1), May 2020. doi: 10.1038/s41598-020-65412-3.

DeMets, C., Gordon, R. G., Argus, D. F., and Stein, S. Current plate motions. *Geophysical Journal International*, 101(2):425–478, May 1990. doi: 10.1111/j.1365-246x.1990.tb06579.x.

Dorbath, L., Cisternas, A., and Dorbath, C. Assessment of the size of large and great historical earthquakes in Peru. *Bulletin of the Seismological Society of America*, 80(3):551–576, 06 1990. doi: 10.1785/BSSA0800030551.

Drápela, J., Calisto, I., and Moreno, M. Locking-derived tsunami scenarios for the most recent megathrust earthquakes in Chile: implications for tsunami hazard assessment. *Natural Hazards*, 107(1):35–52, Jan. 2021. doi: 10.1007/s11069-021-04572-5.

Dura, T., Cisternas, M., Horton, B. P., Ely, L. L., Nelson, A. R., Wesson, R. L., and Pilarczyk, J. E. Coastal evidence for Holocene subduction-zone earthquakes and tsunamis in central Chile. *Quaternary Science Reviews*, 113:93–111, Apr. 2015. doi: 10.1016/j.quascirev.2014.10.015.

Dziewonski, A. M. and Anderson, D. L. Preliminary reference Earth model. *Physics of the Earth and Planetary Interiors*, 25(4): 297–356, June 1981. doi: 10.1016/0031-9201(81)90046-7.

Ely, L. L., Cisternas, M., Wesson, R. L., and Dura, T. Five centuries of tsunamis and land-level changes in the overlapping rupture area of the 1960 and 2010 Chilean earthquakes. *Geology*, 42(11): 995–998, Nov. 2014. doi: 10.1130/g35830.1.

Flanders Marine Institute (VLIZ), Belgium and Intergovernmental Oceanographic Commission-UNESCO, France. Sea level station monitoring facility, 2021. doi: 10.14284/482.

Fritz, H. M., Petroff, C. M., Catalán, P. A., Cienfuegos, R., Winckler, P., Kalligeris, N., Weiss, R., Barrientos, S. E., Meneses, G., Valderas-Bermejo, C., Ebeling, C., Papadopoulos, A., Contreras, M., Almar, R., Dominguez, J. C., and Synolakis, C. E. Field Survey of the 27 February 2010 Chile Tsunami. *Pure and Applied Geophysics*, 168 (11):1989–2010, Mar. 2011. doi: 10.1007/s00024-011-0283-5.

GFZ German Research Centre For Geosciences and Institut Des Sciences De L'Univers-Centre National De La Recherche CNRS-INSU. IPOC Seismic Network, 2006. doi: 10.14470/PK615318.

Goda, K., Yasuda, T., Mori, N., and Maruyama, T. New Scaling Relationships of Earthquake Source Parameters for Stochastic Tsunami Simulation. *Coastal Engineering Journal*, 58(3):1650010–1–1650010–40, Sept. 2016. doi: 10.1142/s0578563416500108.

Gusman, A. R., Murotani, S., Satake, K., Heidarzadeh, M., Gunawan, E., Watada, S., and Schurr, B. Fault slip distribution of the 2014 Iquique, Chile, earthquake estimated from ocean-wide tsunami waveforms and GPS data. *Geophysical Research Letters*, 42(4): 1053–1060, Feb. 2015. doi: 10.1002/2014gl062604.

Hayes, G. P. The finite, kinematic rupture properties of great-sized earthquakes since 1990. *Earth and Planetary Science Letters*, 468:94–100, June 2017. doi: 10.1016/j.epsl.2017.04.003.

Hayes, G. P., Herman, M. W., Barnhart, W. D., Furlong, K. P., Riquelme, S., Benz, H. M., Bergman, E., Barrientos, S., Earle, P. S., and Samsonov, S. Continuing megathrust earthquake potential in Chile after the 2014 Iquique earthquake. *Nature*, 512 (7514):295–298, Aug. 2014. doi: 10.1038/nature13677.

Hayes, G. P., Moore, G. L., Portner, D. E., Hearne, M., Flamme, H., Furtney, M., and Smoczyk, G. M. Slab2, a comprehensive subduction zone geometry model. *Science*, 362(6410):58–61, 2018. doi: 10.1126/science.aat4723.

Herrera, M. T., Crempien, J. G. F., Cembrano, J., and Moreno, M. Seismic cycle controlled by subduction geometry: novel 3-D quasi-dynamic model of Central Chile megathrust. *Geophysical Journal International*, 237(2):772–787, Feb. 2024. doi: 10.1093/gji/ggae069.

Herrero, A. and Bernard, P. A kinematic self-similar rupture process for earthquakes. *Bulletin of the Seismological Society of America*, 84(4):1216–1228, Aug. 1994. doi: 10.1785/bssa0840041216.

Kajiura, K. The leading edge of a Tsunami. *Bulletin of the Earthquake Research Institute, University of Tokyo*, 41:535–571, 1963.

Lay, T., Ammon, C. J., Kanamori, H., Xue, L., and Kim, M. J. Possible large near-trench slip during the 2011 M w 9.0 off the Pacific coast of Tohoku Earthquake. *Earth, Planets and Space*, 63(7): 687–692, July 2011. doi: 10.5047/eps.2011.05.033.

LeVeque, R. J., Waagan, K., González, F. I., Rim, D., and Lin, G. Generating Random Earthquake Events for Probabilistic Tsunami Hazard Assessment. *Pure and Applied Geophysics*, 173(12): 3671–3692, Aug. 2016. doi: 10.1007/s00024-016-1357-1.

Li, S., Moreno, M., Bedford, J., Rosenau, M., and Oncken, O. Revisiting viscoelastic effects on interseismic deformation and locking degree: A case study of the Peru-North Chile subduction zone. *Journal of Geophysical Research: Solid Earth*, 120(6):4522–4538, 2015. doi: 10.1002/2015JB011903.

Li, Y., Shan, X., Gao, Z., and Qu, C. Interseismic Coupling–Based Stochastic Slip Modeling of the 1920 Ms 8.5 Haiyuan Earthquake. *Seismological Research Letters*, 95(2A):870–878, Nov. 2023. doi: 10.1785/0220230253.

Lomnitz, C. Major Earthquakes of Chile: A Historical Survey, 1535-1960. *Seismological Research Letters*, 75(3):368–378, May 2004. doi: 10.1785/gssrl.75.3.368.

Lorito, S., Romano, F., Atzori, S., Tong, X., Avallone, A., McCloskey, J., Cocco, M., Boschi, E., and Piatanesi, A. Limited overlap between the seismic gap and coseismic slip of the great 2010 Chile earthquake. *Nature Geoscience*, 4(3):173–177, Jan. 2011. doi: 10.1038/ngeo1073.

Loveless, J. P. and Meade, B. J. Spatial correlation of interseismic coupling and coseismic rupture extent of the 2011 MW= 9.0 Tohoku-oki earthquake. *Geophysical Research Letters*, 38(17), Sept. 2011. doi: 10.1029/2011gl048561.

Loveless, J. P. and Meade, B. J. Two decades of spatiotemporal variations in subduction zone coupling offshore Japan. *Earth and Planetary Science Letters*, 436:19–30, 2016. doi: 10.1016/j.epsl.2015.12.033.

Mai, P. M. and Beroza, G. C. A spatial random field model to characterize complexity in earthquake slip. *Journal of Geophysical Research: Solid Earth*, 107(B11):ESE 10–1–ESE 10–21, 2002. doi: https://doi.org/10.1029/2001JB000588.

Maksymowicz, A., Tréhu, A. M., Contreras-Reyes, E., and Ruiz, S. Density-depth model of the continental wedge at the maximum slip segment of the Maule Mw8.8 megathrust earthquake. *Earth and Planetary Science Letters*, 409:265–277, Jan. 2015. doi: 10.1016/j.epsl.2014.11.005.

Melgar, D. and Hayes, G. P. The Correlation Lengths and Hypocentral Positions of Great Earthquakes. *Bulletin of the Seismological Society of America*, 109(6):2582–2593, Nov. 2019. doi: 10.1785/0120190164.

Melgar, D., Williamson, A. L., and Salazar-Monroy, E. F. Differences between heterogenous and homogenous slip in regional tsunami hazards modelling. *Geophysical Journal International*, 219(1):553–562, 07 2019. doi: 10.1093/gji/ggz299.

Met Office. *Cartopy: a cartographic python library with a Matplotlib interface*. Exeter, Devon, 2010 - 2015. http://scitools.org.uk/cartopy.

Molina, D., Tassara, A., Abarca, R., Melnick, D., and Madella, A. Frictional Segmentation of the Chilean Megathrust From a Multivariate Analysis of Geophysical, Geological, and Geodetic Data. *Journal of Geophysical Research: Solid Earth*, 126(6), June 2021. doi: 10.1029/2020jb020647.

Moreno, M., Rosenau, M., and Oncken, O. 2010 Maule earthquake slip correlates with pre-seismic locking of Andean subduction zone. *Nature*, 467(7312):198–202, Sept. 2010. doi: 10.1038/nature09349.

Métois, M., Vigny, C., and Socquet, A. Interseismic Coupling, Megathrust Earthquakes and Seismic Swarms Along the Chilean Subduction Zone (38°–18°S). *Pure and Applied Geophysics*, 173 (5):1431–1449, Apr. 2016. doi: 10.1007/s00024-016-1280-5.

Nealy, J. L., Herman, M. W., Moore, G. L., Hayes, G. P., Benz, H. M., Bergman, E. A., and Barrientos, S. E. 2017 Valparaíso earthquake sequence and the megathrust patchwork of central Chile. *Geophysical Research Letters*, 44(17):8865–8872, Sept. 2017. doi: 10.1002/2017gl074767.

Okada, Y. Surface deformation due to shear and tensile faults in a half-space. *Bulletin of the Seismological Society of America*, 75 (4):1135–1154, Aug. 1985. doi: 10.1785/bssa0750041135.

Okuwaki, R., Yagi, Y., Aránguiz, R., González, J., and González, G. Rupture Process During the 2015 Illapel, Chile Earthquake: Zigzag-Along-Dip Rupture Episodes. *Pure and Applied Geophysics*, 173(4):1011–1020, 2016. doi: 10.1007/s00024-016-1271-6.

Philibosian, B. and Meltzner, A. J. Segmentation and supercycles: A catalog of earthquake rupture patterns from the Sumatran Sunda Megathrust and other well-studied faults worldwide. *Quaternary Science Reviews*, 241:106390, Aug. 2020. doi: 10.1016/j.quascirev.2020.106390.

Protti, M., González, V., Newman, A. V., Dixon, T. H., Schwartz, S. Y., Marshall, J. S., Feng, L., Walter, J. I., Malservisi, R., and Owen, S. E. Nicoya earthquake rupture anticipated by geodetic measurement of the locked plate interface. *Nature Geoscience*, 7(2): 117–121, Dec. 2013. doi: 10.1038/ngeo2038.

Romano, F., Piatanesi, A., Lorito, S., Tolomei, C., Atzori, S., and Murphy, S. Optimal time alignment of tide-gauge tsunami waveforms in nonlinear inversions: Application to the 2015 Illapel (Chile) earthquake. *Geophysical Research Letters*, 43(21), Nov. 2016. doi: 10.1002/2016gl071310.

Ruiz, J. A., Fuentes, M., Riquelme, S., Campos, J., and Cisternas, A. Numerical simulation of tsunami runup in northern Chile based on non-uniform k-2 slip distributions. *Natural Hazards*, 79(2): 1177–1198, Aug. 2015. doi: 10.1007/s11069-015-1901-9.

Ruiz, J. A., Contreras-Reyes, E., Ortega-Culaciati, F., and Manríquez, P. Rupture process of the April 24, 2017, Mw 6.9 Valparaíso earthquake from the joint inversion of teleseismic body waves and near-field data. *Physics of the Earth and Planetary Interiors*, 279:1–14, June 2018. doi: 10.1016/j.pepi.2018.03.007.

Ruiz, S. and Madariaga, R. Historical and recent large megathrust earthquakes in Chile. *Tectonophysics*, 733:37–56, May 2018. doi: 10.1016/j.tecto.2018.01.015.

Ruiz, S., Metois, M., Fuenzalida, A., Ruiz, J., Leyton, F., Grandin, R., Vigny, C., Madariaga, R., and Campos, J. Intense foreshocks and a slow slip event preceded the 2014 Iquique M w 8.1 earthquake. *Science*, 345(6201):1165–1169, Sept. 2014. doi: 10.1126/science.1256074.

Ruiz, S., Aden-Antoniow, F., Baez, J. C., Otarola, C., Potin, B., del Campo, F., Poli, P., Flores, C., Satriano, C., Leyton, F., Madariaga, R., and Bernard, P. Nucleation Phase and Dynamic Inversion of the Mw 6.9 Valparaíso 2017 Earthquake in Central Chile. *Geophysical Research Letters*, 44(20), Oct. 2017. doi: 10.1002/2017gl075675.

San Martín, J., Calisto, I., Quezada, J., Stewart, D., Ely, L., Cifuentes-Lobos, R., and Moreno, M. Characterization of historical megathrust earthquake ruptures in Central Chile using logic tree analysis. *Natural Hazards*, 120(6):5411–5427, Feb. 2024. doi: 10.1007/s11069-024-06404-8.

Schurr, B., Asch, G., Hainzl, S., Bedford, J., Hoechner, A., Palo, M., Wang, R., Moreno, M., Bartsch, M., Zhang, Y., Oncken, O., Tilmann, F., Dahm, T., Victor, P., Barrientos, S., and Vilotte, J.-P. Gradual unlocking of plate boundary controlled initiation of the 2014 Iquique earthquake. *Nature*, 512(7514):299–302, Aug. 2014. doi: 10.1038/nature13681.

Small, D. T. and Melgar, D. Geodetic Coupling Models as Constraints on Stochastic Earthquake Ruptures: An Example Application to PTHA in Cascadia. *Journal of Geophysical Research: Solid Earth*, 126(7), July 2021. doi: 10.1029/2020jb021149.

Small, D. T. and Melgar, D. Can Stochastic Slip Rupture Modeling Produce Realistic M 9+ Events? *Journal of Geophysical Research: Solid Earth*, 128(3), Mar. 2023. doi: 10.1029/2022jb025716.

Strasser, F. O., Arango, M. C., and Bommer, J. J. Scaling of the Source Dimensions of Interface and Intraslab Subduction-zone Earthquakes with Moment Magnitude. *Seismological Research Letters*, 81(6):941–950, Nov. 2010. doi: 10.1785/gssrl.81.6.941.

Tanioka, Y. and Satake, K. Tsunami generation by horizontal displacement of ocean bottom. *Geophysical Research Letters*, 23 (8):861–864, Apr. 1996. doi: 10.1029/96gl00736.

Vigny, C. and Klein, E. The 1877 megathrust earthquake of North Chile two times smaller than thought? A review of ancient articles. *Journal of South American Earth Sciences*, 117:103878, Aug. 2022. doi: 10.1016/j.jsames.2022.103878.

Vigny, C., Socquet, A., Peyrat, S., Ruegg, J.-C., Métois, M., Madariaga, R., Morvan, S., Lancieri, M., Lacassin, R., Campos, J., Carrizo, D., Bejar-Pizarro, M., Barrientos, S., Armijo, R., Aranda, C., Valderas-Bermejo, M.-C., Ortega, I., Bondoux, F., Baize, S., Lyon-Caen, H., Pavez, A., Vilotte, J. P., Bevis, M., Brooks, B., Smalley, R., Parra, H., Baez, J.-C., Blanco, M., Cimbaro, S., and Kendrick, E. The 2010 M w 8.8 Maule Megathrust Earthquake of Central Chile, Monitored by GPS. *Science*, 332(6036):1417–1421, June 2011. doi: 10.1126/science.1204132.

Wei, S. Source Models of Large Earthquakes: 04/01/2014 (Mw 8.1), Iquique, Chile. http://www.tectonics.caltech.edu/slip_history/2014_chile/index.html, 2014. Accessed November 2026.

Winckler, P., Sepúlveda, I., Aron, F., and Contreras-López, M. How Do Tides and Tsunamis Interact in a Highly Energetic Channel? The Case of Canal Chacao, Chile. *Journal of Geophysical Research: Oceans*, 122(12):9605–9624, Dec. 2017. doi: 10.1002/2017jc012680.

Yue, H., Lay, T., Rivera, L., An, C., Vigny, C., Tong, X., and Báez Soto, J. C. Localized fault slip to the trench in the 2010 Maule, Chile Mw = 8.8 earthquake from joint inversion of high-rate GPS, teleseismic body waves, InSAR, campaign GPS, and tsunami observations. *Journal of Geophysical Research: Solid Earth*, 119(10): 7786–7804, Oct. 2014. doi: 10.1002/2014jb011340.

Zhu, Y., An, C., Yu, H., Zhang, W., and Chen, X. High-resolution tsunami hazard assessment for the Guangdong-Hong Kong-Macao Greater Bay Area based on a non-hydrostatic tsunami model. *Science China Earth Sciences*, 67(7):2326–2351, June 2024. doi: 10.1007/s11430-023-1300-9.

The article *Improving Tsunamigenic Source Models through Interseismic Coupling Approach in Stochastic Slip Distributions: Insights from Large Chilean Earthquakes* © 2026 by Alex Villarroel is licensed under CC BY 4.0.